

## Redox Conditions in the Solar Nebula: Observational, Experimental, and Theoretical Constraints

**Lawrence Grossman**

*Department of the Geophysical Sciences and Enrico Fermi Institute  
The University of Chicago  
Chicago, Illinois 60637, U.S.A.  
yosi@midway.uchicago.edu*

**John R. Beckett**

*Division of Geological and Planetary Sciences  
California Institute of Technology  
Pasadena, California 91125, U.S.A.*

**Alexei V. Fedkin, Steven B. Simon**

*Department of the Geophysical Sciences  
The University of Chicago  
Chicago, Illinois 60637, U.S.A.*

**Fred J. Ciesla**

*Department of Terrestrial Magnetism  
Carnegie Institution of Washington  
Washington, D.C. 20015-1305, U.S.A.*

### ABSTRACT

Crystallization experiments on liquids with compositions similar to those of compact Type A, Type B1 and Type B2 refractory inclusions were conducted under controlled temperature and  $f_{O_2}$  conditions. Application of the results to the compositions of coexisting  $Ti^{3+}$ -bearing fassaite clinopyroxene + melilite pairs in natural inclusions shows that, if they crystallized at ~1509 K, they did so at  $\log f_{O_2} = -19.8 \pm 0.9$ , only slightly below the equilibrium  $\log f_{O_2}$  of a partially condensed system of solar composition at the same temperature,  $-18.1^{+0.2}_{-0.3}$ , or IW-6.8. Fassaite is the only  $f_{O_2}$  indicator that shows that anything in chondrites formed in a system that was close to solar in composition. Solar composition is so reducing that equilibrium calculations predict vanishingly small FeO/(FeO + MgO) ratios in the condensate until temperatures fall below 800 K, where significant oxidation of metallic iron and formation of fayalite in solid solution with previously condensed forsterite begin. The mechanism for the latter process is diffusion of  $Fe^{2+}$  through forsterite, but the diffusion rate is nearly zero at these temperatures. By comparison to what is achievable in a system of solar composition, the mean FeO/(FeO + MgO) ratio of the olivine in chondrules in unequilibrated ordinary chondrites (UOCs) is very high, ~0.15. Making such ratios in chondrule precursors by solar nebular processes requires sufficiently high  $f_{O_2}$  for iron to become oxidized above temperatures where diffusion of  $Fe^{2+}$  becomes very slow. Two dynamic models for enrichment of oxygen relative to carbon and hydrogen were investigated quantitatively: radial transport of water ice-rich migrators across the snow line into the inner part of the solar nebula where the ice evaporates; and coagulation, vertical settling and evaporation of anhydrous dust in the median plane of the inner nebula. In both cases, the maximum achievable  $f_{O_2}$ , ~IW-4.5, produces a maximum  $X_{Fe}$  before diffusion

ceases that is a factor of  $>7$  less than would be required for UOC chondrule precursors, even for grains only  $0.1\ \mu\text{m}$  in radius and nebular cooling times as high as  $10^6$  yr. The same dynamic models are also incapable of creating environments sufficiently oxidizing to produce olivine with  $X_{\text{Fa}} = 0.15$  during formation of chondrules by melting of FeO-poor precursors. If, instead, chondrule precursors were made of very FeO-rich, non-equilibrium condensates, reduction of chondrule melts by nebular gas may have been arrested before the mean  $X_{\text{Fa}}$  of chondrule olivine could fall below 0.15 because chondrules were hot for such a short time. A nebular origin for the mineral assemblage of unequilibrated enstatite chondrites (UECs) requires  $f_{\text{O}_2}$  significantly below that of a system of solar composition. In particular, after fractionation of specific amounts of predicted high-temperature condensates, equilibrium condensation in a system whose  $P^{\text{tot}} = 10^{-4}$  atm and whose initial composition is solar except for a C/O ratio of 0.83 yields an assemblage characterized by a very large enstatite/forsterite ratio, the presence of oldhamite and niningerite, metallic nickel-iron containing several wt% Si, and small amounts of pure silica and albitic plagioclase, very similar to the mineral assemblage of EH3 chondrites. Log  $f_{\text{O}_2}$  in this system varies from IW-8.9 at 1500 K to IW-13 at 900 K. The mechanisms proposed to date for fractionation of C, O and H from one another are quantitatively insufficient to produce the magnitude of nebular  $f_{\text{O}_2}$  variations needed to account for primitive features of UOCs and UECs.

## INTRODUCTION

Chondrites formed in the solar nebula. Although most were modified by metamorphic processes in the parent bodies into which they accreted, a common theme of studies of the least metamorphosed chondrites is that they possess mineralogical, chemical and isotopic characteristics inherited from the solar nebula at the time of their formation. If such characteristics are interpreted correctly, they can be unique and valuable clues to the composition of and physico-chemical conditions in the solar nebular region where they formed. One such characteristic is the relative amount of a particular element in each of two or more oxidation states in a given mineral assemblage. This is a direct measure of the equilibrium partial pressure of oxygen, or oxygen fugacity,  $f_{\text{O}_2}$ , of the gas with which the assemblage may have equilibrated, in this case, the gas in the region of the solar nebula where the assemblage formed. The  $f_{\text{O}_2}$  is largely determined by the relative abundances of carbon, oxygen and hydrogen in cosmic gases. In this work, an experimental calibration of the relationship between  $f_{\text{O}_2}$  and the  $\text{Ti}^{3+}/\text{Ti}^{4+}$  ratio of pyroxene is determined and used to infer the  $f_{\text{O}_2}$  of the gas with which coexisting melilite and pyroxene equilibrated when they crystallized from melt droplets to form refractory inclusions. This  $f_{\text{O}_2}$  is well below that required to produce the mean fayalite content of olivine in chondrules in unequilibrated ordinary chondrites (UOCs). Fractionations of oxygen from carbon and hydrogen resulting from two dynamic nebular processes, radial transport of water ice-bearing migrators, followed by evaporation of the ice; and coagulation, vertical settling and evaporation of anhydrous dust, are investigated quantitatively to see if they can produce the inferred  $f_{\text{O}_2}$  variation. Finally, the  $f_{\text{O}_2}$  of the gas is determined that can account for the distribution of silicon between metal and silicates, and of calcium and magnesium between sulfides and silicates, in EH3 chondrites by condensation.

## OXYGEN FUGACITY DURING CRYSTALLIZATION OF REFRACTORY INCLUSION MELTS

### Experimental technique

Synthesis experiments were conducted in S. E. Haggerty's laboratory at the University of Massachusetts. Starting compositions for melting experiments were obtained by weighing and mixing  $\text{CaCO}_3$  (Baker's ACS),  $\text{MgO}$  (Muscle Shoal's Electrode Co. or ALFA Puratonic),  $\text{Al}_2\text{O}_3 \cdot 3\text{H}_2\text{O}$  (Fisher Certified Reagent) or  $\text{Al}_2\text{O}_3$  (ALFA Puratonic),  $\text{SiO}_2$  (optical grade quality

quartz crushed to -200 mesh or ALFA Puratonic), and  $\text{TiO}_2$  (Baker's Analyzed Reagent). These mixtures were ground under ethanol by hand in an agate mortar for one hour, in an automatic agate mortar for 2-3 hours and allowed to dry in a drying oven or in air overnight. The oxide mixes were placed in a Pt crucible, brought to 1000 °C in stages over a period of one day and held there for 2-3 days. They were then heated in air, either in a Pt-wound resistance furnace or in a Del Tech VT-31 furnace at ~1300 °C for several hours. The samples were placed in a Pt crucible that was suspended at the end of an alumina rod into the hot spot of the furnace. Samples were quenched by removing a plug from the bottom port of the furnace, detaching the sample holder from a brass fitting at the top of the furnace and dropping the sample holder and crucible through the furnace onto a block of ice beneath the bottom port. The glasses so produced were analyzed by electron microprobe, and the three starting compositions used in this work are shown in Table 1. Spinel crystals were not observed. The bulk compositions of B1-1 and B2-1 represent attempts at producing charges having the same bulk compositions as TS33 and TS20, specific examples of Type B1 and Type B2 inclusions, respectively. Both are clinopyroxene-rich types of refractory inclusions found in CV3 chondrites, the former having more normative melilite due to their lower  $\text{SiO}_2$  contents than the latter. The bulk composition of ETEG was chosen to be undersaturated with respect to spinel and to yield large amounts of clinopyroxene having high  $\text{Ti}_2\text{O}_3$  contents. This bulk composition does not correspond to that of any particular inclusion, and is much lower in MgO and  $\text{Al}_2\text{O}_3$  and much higher in  $\text{SiO}_2$  and  $\text{TiO}_2$  than all Type B inclusions (Simon and Grossman 2004).

**Table 1.** Bulk compositions studied in this work (wt%).

	B1-1	B2-1	ETEG
MgO	8.5	12.0	6.4
$\text{Al}_2\text{O}_3$	31.8	28.3	19.2
$\text{SiO}_2$	27.6	32.9	37.4
CaO	28.1	24.7	30.8
$\text{TiO}_2$	4.0	2.1	6.5
Total	100.0	100.0	100.3

For quenching experiments, a vertical Del Tech VT-31 furnace was used, together with a Eurotherm model 90 temperature controller. Temperatures were measured with a Pt-Pt10Rh type S thermocouple calibrated against an NBS calibrated type S thermocouple and against the melting points of ITS-90 Au and Ni (1064.18 and 1455 °C, respectively). The gas mixing system is a slight modification of that designed by Williams and Mullins (1976). A mullite reaction tube was inserted into the furnace, and the gas mix was introduced through a gas inlet at the top. Chips of glass starting material were placed into cages made of 0.12 mm Ir wire, which were suspended from a long alumina rod. While the sample holder port at the top of the furnace was temporarily plugged, the furnace temperature was adjusted to within a few degrees of the desired temperature. The gas mix was then introduced at a flow rate that gave a positive pressure within the reaction tube. After minor adjustments of flow rate and temperature, the plug was removed, and the sample holder assembly was inserted through the port such that the sample was in the hot spot of the furnace adjacent to the thermocouple. Air is introduced at this time, but it was found that the  $f_{\text{O}_2}$  at the sample site stabilized after 10-15 minutes. Samples were first placed in the experimental gas mix at a temperature 10-40 degrees above that of the first appearance of clinopyroxene for 1-2 hours, allowing the  $\text{Ti}^{3+}/\text{Ti}^{4+}$  ratio of the melt to equilibrate with the gas mix. The furnace temperature was then reduced to the run condition temperature. Runs were terminated by quenching into a beaker of water by removing a plug at the base of the furnace, and passing an electric current through the Ir wire holding the sample cage to the alumina rod.

A horizontal, Kanthal wound, model 1201 Marshall furnace was used for some calibration experiments. Temperature was controlled to  $\pm 2$  °C by a Marshall model 4045 temperature controller, resulting in a hot spot that varied by no more than  $\pm 3$  °C over a three inch length. Temperatures were measured as in the Del Tech furnace.

Low  $f_{O_2}$  was achieved by bubbling a gas with 15 vol%  $H_2$  and 85 vol%  $N_2$  through two polyethylene bottles containing a concentrated sulfuric acid solution. A plug of glass wool was inserted into the tubing beyond the point where the gas had passed through the acid baths, in order to prevent sulfuric acid droplets in the gas stream from entering the furnace. The gas mix was nonexplosive due to dilution of  $H_2$  in the  $N_2$  carrier gas. Since a slightly positive total pressure,  $P^{tot}$ , ( $\sim 1$  atm) was maintained in the gas system, the partial pressure of  $H_2$ ,  $P_{H_2}$ , in the  $N_2$ - $H_2$  gas mix was 0.15 atm. The partial pressure of  $H_2O$ ,  $P_{H_2O}$ , over the sulfuric acid was fixed by the temperature of the acid bath ( $24 \pm 1$  °C) and the concentration of  $H_2O$  in the acid. Oxygen fugacities were found to be independent of flow rate between 125 and 1000 ml/min, as measured at ambient temperature. A rate of 500-1000 ml/min was used in the experiments. This generated a specific  $H_2/H_2O$  volume ratio in the gas and buffered the oxygen fugacity of the gas mix used in the experiments. All experiments were conducted using aliquots from the same master batch of sulfuric acid solution. No significant change in either the  $H_2O$  content of the acid bath or in measured  $H_2/H_2O$  ratios in the resulting gas was observed. The acid bath was changed every two weeks when continuous experimentation was conducted.

The densities of the sulfuric acid solutions were measured by weighing known volumes of acid before and after each batch of acid was changed. The density obtained,  $1.805 \pm 0.008$  g/cm<sup>3</sup>, corresponds to 10-12 wt%  $H_2O$  (Perry and Chilton 1973). Taking the range of  $P_{H_2O}$  in equilibrium with sulfuric acid solutions with this range of water contents at 24 °C (Perry and Chilton 1973) and assuming  $P_{H_2} = 0.15$  atm gives  $P_{H_2}/P_{H_2O}$  of  $11100 \pm 3500$ . The oxygen fugacity of an  $H_2$ - $H_2O$  gas mix is governed by the equilibrium  $H_{2(g)} + 1/2 O_{2(g)} = H_2O_{(g)}$ . Using the data in Chase (1998) for the free energy of this reaction, the experimental gas mix has  $\log f_{O_2} = -19.5 \pm 0.3$  at 1500 K. In another calibration study, the reaction  $2Cr_{(s)} + 3/2 O_{2(g)} = Cr_2O_{3(s)}$  was reversed in the experimental gas mix in the Marshall furnace between 908 and 951 °C. Powdered Cr or  $Cr_2O_3$  was placed in a mullite boat attached to a thermocouple well by Pt wires. The thermocouple well and sample were in the cooler part of the furnace, 100-200 °C, while the furnace was brought up to the desired run temperature, and the gas allowed to equilibrate; they were then pushed into the hot spot where they were held in the experimental gas stream for four days. Quenching was accomplished by pulling the thermocouple well back into the cooler part of the furnace, during which the temperature of the sample fell from the run temperature to under  $\sim 300$  °C in less than three minutes. The furnace was then brought to room temperature over several hours, and the sample removed. Zero time experiments, in which samples were quenched immediately after the thermocouple indicated that the run temperature had been achieved, demonstrated that significant reaction occurred neither during introduction of the sample nor during quenching for run temperatures between 700 and 1000 °C. Holzheid and O'Neill (1995) used electrochemical measurements to determine the chemical potential of  $O_{2(g)}$  in equilibrium with  $Cr_{(c)}$  and  $Cr_2O_{3(c)}$  as a function of temperature. Setting  $RT \ln f_{O_2}$  equal to their chemical potential leads to the conclusion that  $\log f_{O_2}$  in the experimental gas mix was greater than  $-24.1$  at 908 °C and less than  $-23.0$  at 951 °C. Using these limits on the equilibrium  $\log f_{O_2}$  yields  $6400 < P_{H_2}/P_{H_2O} < 9900$ . For such a gas mix,  $-19.4 < \log f_{O_2} < -19.1$  at 1500 K.

Phase compositions in run products were determined with an automated ARL-EMX-SM three-spectrometer electron microprobe operated at a voltage of 15 keV and a beam current of either 0.25 to 0.6  $\mu A$  for wavelength dispersive analyses or 0.1  $\mu A$  for energy dispersive analyses. Standards used were Ilm-A128 for Fe and Ti, An 100 glass for Ca and Si, En 100 glass for Mg, and  $Al_2O_3$  for Al. On-line data reduction employed the program MAGIC (JW Colby, Bell Laboratories) for wavelength dispersive analyses, and a procedure modified from that of Reed and Ware (1973) for energy dispersive analyses.

## Results

Results for all successful runs are summarized in Table 2, in which  $\log f_{O_2}$  is based on the  $P_{H_2}/P_{H_2O}$  ratio of the gas mix determined from Cr-  $Cr_2O_3$  equilibrium.

Average glass compositions for five of the runs are shown in Table 3. The relatively low MgO and high TiO<sub>2</sub> contents of the ETEG bulk composition relative to those of Type B inclusions are reflected in the differences in glass compositions between the ETEG runs and those of the other bulk compositions studied. Average melilite compositions and their standard deviations are shown for each of the run products in Table 4. Melilite is a solid solution between gehlenite (Ge), Ca<sub>2</sub>Al<sub>2</sub>SiO<sub>7</sub>, and åkermanite (Åk), Ca<sub>2</sub>MgSi<sub>2</sub>O<sub>7</sub>. As seen in Table 4, the average mole fraction åkermanite,  $X_{\text{Åk}}$ , ranges from 0.36 to 0.67 in the run products, with melilite from the bulk composition with the lowest MgO/Al<sub>2</sub>O<sub>3</sub> ratio, B1-1, having the lowest  $X_{\text{Åk}}$ . In the B2-1 runs, the average  $X_{\text{Åk}}$  of melilite increases with decreasing equilibration temperature, but this relationship is not found in the ETEG runs.

Synthetic clinopyroxene has a pale green to blue-green pleochroism which is more intense in the pyroxene from ETEG and B1-1 runs than in that from B2-1 runs, which is lower in Ti content. The fact that clinopyroxene synthesized at low  $f_{\text{O}_2}$ , and containing negligible amounts of multivalent elements except for Ti, exhibits pleochroism suggests the presence of both Ti<sup>3+</sup> and Ti<sup>4+</sup>. This is further indicated by the similarity of the pleochroism and compositions of the

Table 2. Run conditions and results.

Run	Bulk Composition	$T$ (°C)	$\log f_{\text{O}_2}$ (atm)	Time (hr)	Mineral Assemblage
83L-37	B1-1	1229	$-19.2 \pm 0.2$	63	Sp, Mel, Cpx, An, gl
83L-33	B2-1	1244	$-19.1 \pm 0.2$	17	Sp, Mel, Cpx, An, gl
83L-34	B2-1	1236	$-19.2 \pm 0.2$	13	Sp, Mel, Cpx, An, gl
83L-17	ETEG	1229	$-19.2 \pm 0.2$	22	Cpx, Mel, An, Pv, gl
83L-18	ETEG	1221	$-19.3 \pm 0.2$	26	Cpx, Mel, An, Pv, gl
83L-19	ETEG	1209	$-19.5 \pm 0.2$	24	Cpx, Mel, An, Pv, gl

Sp: spinel; Mel: melilite; Cpx: fassaite; An: anorthite; gl: glass; Pv: perovskite.

Table 3. Compositions of synthetic glass.

Run	83L-37	83L-33	83L-17	83L-18	83L-19
MgO (wt%)	$5.80 \pm 0.11$	$8.50 \pm 0.02$	$4.67 \pm 0.01$	$5.94 \pm 0.14$	$3.82 \pm 0.07$
Al <sub>2</sub> O <sub>3</sub>	$21.96 \pm 0.57$	$18.72 \pm 0.37$	$16.66 \pm 0.29$	$15.05 \pm 0.09$	$14.45 \pm 0.13$
SiO <sub>2</sub>	$40.53 \pm 0.79$	$41.08 \pm 0.29$	$40.13 \pm 0.12$	$40.38 \pm 0.86$	$39.86 \pm 0.34$
CaO	$28.60 \pm 0.02$	$29.50 \pm 0.24$	$32.47 \pm 0.16$	$31.94 \pm 0.61$	$35.29 \pm 0.65$
TiO <sub>2</sub>	$1.86 \pm 0.15$	$2.13 \pm 0.18$	$5.12 \pm 0.11$	$6.82 \pm 0.51$	$5.97 \pm 0.09$
FeO	$0.03 \pm 0.00$	$0.01 \pm 0.01$	$0.03 \pm 0.01$	$0.03 \pm 0.02$	$0.01 \pm 0.01$
Total	$98.78 \pm 0.49$	$99.94 \pm 0.75$	$99.08 \pm 0.49$	$100.16 \pm 0.90$	$99.40 \pm 0.50$
<b>Cation Proportions</b>					
Mg	$0.081 \pm 0.001$	$0.116 \pm 0.001$	$0.066 \pm 0.000$	$0.083 \pm 0.002$	$0.054 \pm 0.001$
Al	$0.242 \pm 0.007$	$0.202 \pm 0.002$	$0.187 \pm 0.003$	$0.167 \pm 0.004$	$0.162 \pm 0.002$
Si	$0.378 \pm 0.006$	$0.377 \pm 0.000$	$0.380 \pm 0.001$	$0.380 \pm 0.006$	$0.380 \pm 0.004$
Ca	$0.286 \pm 0.001$	$0.290 \pm 0.000$	$0.330 \pm 0.001$	$0.322 \pm 0.003$	$0.361 \pm 0.005$
Ti	$0.013 \pm 0.001$	$0.015 \pm 0.001$	$0.037 \pm 0.001$	$0.048 \pm 0.004$	$0.043 \pm 0.001$
Fe	0	$0.001 \pm 0.001$	0	0	0

Uncertainties represent one standard deviation.

**Table 4.** Compositions of synthetic melilite.

Run	83L-37	83L-33	83L-34	83L-17	83L-18	83L-19
MgO (wt%)	5.10 ± 0.35	8.31 ± 0.77	7.76 ± 0.28	8.30 ± 0.28	9.69 ± 1.43	7.14 ± 0.33
Al <sub>2</sub> O <sub>3</sub>	24.47 ± 1.74	17.31 ± 1.16	15.23 ± 0.59	15.92 ± 0.57	12.19 ± 3.73	18.01 ± 0.95
SiO <sub>2</sub>	30.44 ± 1.40	33.27 ± 0.67	35.91 ± 0.18	34.42 ± 0.43	35.69 ± 2.89	33.89 ± 0.94
CaO	40.66 ± 0.40	40.98 ± 0.23	40.63 ± 0.52	40.55 ± 0.31	40.69 ± 0.31	41.21 ± 0.80
TiO <sub>2</sub>	n. d.	n. d.	n. d.	n. d.	0.27 ± 0.13	0.17 ± 0.02
FeO	n. d.	n. d.	n. d.	n. d.	0.08 ± 0.00	0.01 ± 0.01
Total	100.67 ± 1.10	98.87 ± 0.66	99.53 ± 0.69	99.19 ± 0.55	98.61 ± 0.40	100.43 ± 0.93
<b>Cations per 7 Oxygen Anions</b>						
Mg	0.342 ± 0.021	0.565 ± 0.050	0.526 ± 0.022	0.566 ± 0.018	0.663 ± 0.094	0.482 ± 0.022
Al	1.300 ± 0.090	0.931 ± 0.066	0.817 ± 0.026	0.859 ± 0.032	0.665 ± 0.208	0.961 ± 0.050
Si	1.372 ± 0.062	1.518 ± 0.026	1.634 ± 0.015	1.578 ± 0.014	1.651 ± 0.122	1.534 ± 0.042
Ca	1.964 ± 0.021	2.003 ± 0.001	1.981 ± 0.016	1.989 ± 0.006	2.017 ± 0.030	1.999 ± 0.031
Ti	—	—	—	—	0.010 ± 0.005	0.006 ± 0.001
Fe	—	—	—	—	0.001 ± 0.000	0
Total	4.978 ± 0.113	5.017 ± 0.087	4.958 ± 0.041	4.992 ± 0.040	5.007 ± 0.261	4.982 ± 0.052
X <sub>Ak</sub>	0.357 ± 0.050	0.531 ± 3.1	0.600 ± 1.3	0.572 ± 0.016	0.668 ± 0.102	0.523 ± 0.030

n. d.: not detected. Uncertainties represent one standard deviation.

synthetic pyroxene to those of natural pyroxene, called fassaite, in refractory inclusions from the Allende meteorite, which has been shown to contain both Ti<sup>3+</sup> and Ti<sup>4+</sup> on the basis of optical spectroscopy (Dowty and Clark 1973; Burns and Huggins 1973) and X-ray absorption near-edge structure (XANES) spectroscopy (S. Simon et al. 2005). In Table 5, each column shows the average composition of the fassaite in a particular run product, with one standard deviation on the mean of the analyses quoted as the uncertainties. TiO<sub>2</sub><sup>tot</sup> is the wt% TiO<sub>2</sub> when all Ti is calculated as TiO<sub>2</sub>. The entries for TiO<sub>2</sub> and Ti<sub>2</sub>O<sub>3</sub> are the weight percentages of these oxides when the pyroxene formula is calculated on the basis of four total cations, including exactly 1.00 Ca ion, per six oxygen atoms, the result of which is given in the middle section of the table. From such formulae, the pyroxene composition is resolved into the mole fractions of five pyroxene end-members by assigning all Mg to diopside, Di, CaMgSi<sub>2</sub>O<sub>6</sub>; all Fe to hedenbergite, Hd, CaFeSi<sub>2</sub>O<sub>6</sub>; all Ti<sup>4+</sup> to Ti<sup>4+</sup>-bearing pyroxene, T<sub>4</sub>P, CaTiAl<sub>2</sub>O<sub>6</sub>; all Ti<sup>3+</sup> to Ti<sup>3+</sup>-bearing pyroxene, T<sub>3</sub>P, CaTiAlSiO<sub>6</sub>; and the remainder to Ca-Tschermak's molecule, CaTs, CaAl<sub>2</sub>SiO<sub>6</sub>.

The mean composition of synthetic fassaite crystals from each of the experimental runs in Table 1 is plotted in Figure 1, where they are compared to analyses of multiple individual fassaite points in the natural inclusion analogs of B1-1 and B2-1, TS 33 and TS 20, respectively. All electron microprobe data for fassaite and melilite from natural inclusions used in this work are taken from Simon and Grossman (2006), or are unpublished analyses performed by the same technique and on the same instrument at the University of Chicago as in that work. In general, data for the synthetic fassaite, including that from the ETEG bulk composition, fall along the composition trends of fassaite in the natural refractory inclusions. The fassaite compositions in B2-1 lie entirely within the range of fassaite compositions in its natural analog. The B1-1 fassaite, however, is lower in MgO than the lowest MgO data point from TS33 and higher in TiO<sub>2</sub> + Ti<sub>2</sub>O<sub>3</sub> than the highest point for TS33, reflecting the mismatch in bulk composition between this synthetic material and its natural analog. TS33 actually contains 10.3 wt% MgO, 33.6% Al<sub>2</sub>O<sub>3</sub>, 27.4% SiO<sub>2</sub>, 26.6% CaO and 2.06% TiO<sub>2</sub> (Simon and Grossman 2004), ~25%

**Table 5.** Compositions of synthetic fassaite crystals.

Run	83L-37	83L-33	83L-34	83L-17	83L-18	83L-19
MgO (wt%)	6.7 ± 0.32	10.68 ± 1.03	12.24 ± 0.14	8.94 ± 0.71	10.76 ± 1.43	9.19 ± 0.62
Al <sub>2</sub> O <sub>3</sub>	22.90 ± 0.45	16.92 ± 2.15	14.54 ± 0.83	18.84 ± 1.57	17.44 ± 3.06	19.27 ± 1.65
SiO <sub>2</sub>	33.72 ± 1.32	40.64 ± 1.14	44.08 ± 1.55	36.69 ± 1.66	40.11 ± 3.07	35.99 ± 1.44
CaO	24.72 ± 0.12	25.08 ± 0.31	25.70 ± 0.27	24.72 ± 0.36	25.52 ± 0.80	25.28 ± 0.29
TiO <sub>2</sub> <sup>tot</sup>	12.89 ± 1.65	6.56 ± 0.55	4.36 ± 0.52	10.79 ± 0.94	7.49 ± 1.67	9.73 ± 0.95
Ti <sub>2</sub> O <sub>3</sub>	7.86 ± 0.97	2.98 ± 0.82	1.83 ± 0.79	5.57 ± 0.60	2.66 ± 1.31	3.66 ± 0.52
TiO <sub>2</sub>	4.09 ± 0.94	3.23 ± 0.44	2.32 ± 1.39	4.55 ± 0.61	4.52 ± 0.07	5.76 ± 0.64
FeO	0.01 ± 0.01	0.01 ± 0.00	0	0.02 ± 0.02	0.03 ± 0.03	0.01 ± 0.02
Total	100.01 ± 0.97	99.53 ± 0.83	100.71 ± 2.18	99.33 ± 0.57	101.04 ± 0.89	99.15 ± 0.66

Cations in Formula with 4 Total Cations, including 1 Ca Cation, per 6 Oxygen Anions						
Mg	0.374 ± 0.019	0.586 ± 0.059	0.662 ± 0.018	0.498 ± 0.041	0.584 ± 0.083	0.516 ± 0.037
Al	1.007 ± 0.029	0.734 ± 0.096	0.622 ± 0.039	0.829 ± 0.073	0.749 ± 0.137	0.855 ± 0.077
Si	1.258 ± 0.056	1.497 ± 0.061	1.598 ± 0.069	1.370 ± 0.074	1.461 ± 0.136	1.354 ± 0.065
Ti <sup>3+</sup>	0.246 ± 0.031	0.092 ± 0.025	0.056 ± 0.024	0.175 ± 0.019	0.081 ± 0.040	0.114 ± 0.017
Ti <sup>4+</sup>	0.116 ± 0.027	0.090 ± 0.013	0.063 ± 0.038	0.128 ± 0.018	0.124 ± 0.007	0.161 ± 0.019
Fe	0	0	0	0.001 ± 0.001	0.001 ± 0.001	0.001 ± 0.001

Mole Fractions of Pyroxene Components						
Di	0.374 ± 0.019	0.586 ± 0.059	0.662 ± 0.018	0.498 ± 0.041	0.584 ± 0.083	0.515 ± 0.037
CaTs	0.265 ± 0.008	0.232 ± 0.030	0.219 ± 0.014	0.199 ± 0.017	0.210 ± 0.038	0.209 ± 0.019
T <sub>3</sub> P	0.246 ± 0.031	0.092 ± 0.025	0.055 ± 0.024	0.174 ± 0.019	0.081 ± 0.040	0.114 ± 0.017
T <sub>4</sub> P	0.115 ± 0.027	0.090 ± 0.013	0.064 ± 0.038	0.128 ± 0.018	0.124 ± 0.007	0.162 ± 0.019
Hd	0	0	0	0.001 ± 0.001	0.001 ± 0.001	0.001 ± 0.001

Di: CaMgSi<sub>2</sub>O<sub>6</sub>; CaTs: CaAlAlSiO<sub>6</sub>; T<sub>3</sub>P: CaTi<sup>3+</sup>AlSiO<sub>6</sub>; T<sub>4</sub>P: CaTi<sup>4+</sup>Al<sub>2</sub>O<sub>6</sub>; Hd: CaFeSi<sub>2</sub>O<sub>6</sub>. Oxide totals include values for TiO<sub>2</sub> and Ti<sub>2</sub>O<sub>3</sub>, not TiO<sub>2</sub><sup>tot</sup>. Uncertainties are one standard deviation.

higher in MgO and a factor of two lower in TiO<sub>2</sub> than B1-1. Note that all of the synthetic fassaite have Ti<sup>3+</sup>/Ti<sup>tot</sup> ratios between 0.4 and 0.7, the same range as seen for the vast majority of the natural fassaite grains.

Grains of synthetic spinel, anorthite and perovskite large enough to be analyzed without significant contamination from surrounding phases were found to be stoichiometric MgAl<sub>2</sub>O<sub>4</sub>, CaAl<sub>2</sub>Si<sub>2</sub>O<sub>8</sub> and CaTiO<sub>3</sub>, respectively. Spinel contains <0.4 wt% SiO<sub>2</sub>, CaO, TiO<sub>2</sub> and FeO; anorthite <0.2 wt% MgO, TiO<sub>2</sub> and FeO; and perovskite <0.6 wt% MgO, Al<sub>2</sub>O<sub>3</sub>, SiO<sub>2</sub> and TiO<sub>2</sub>.

### Thermochemistry

Three of the run products and most refractory inclusions in CV3 chondrites contain the assemblage melilite, spinel and fassaite, so the equilibrium constants for the following reactions can be obtained from the present study, and used to infer the oxygen fugacities at which the phase assemblages of refractory inclusions equilibrated. The first is



where Sp is spinel, Åk is the åkermanite component of melilite, and T<sub>4</sub>P, T<sub>3</sub>P and Di are the Ti<sup>4+</sup>-bearing, Ti<sup>3+</sup>-bearing and diopside components of clinopyroxene, respectively, and for which



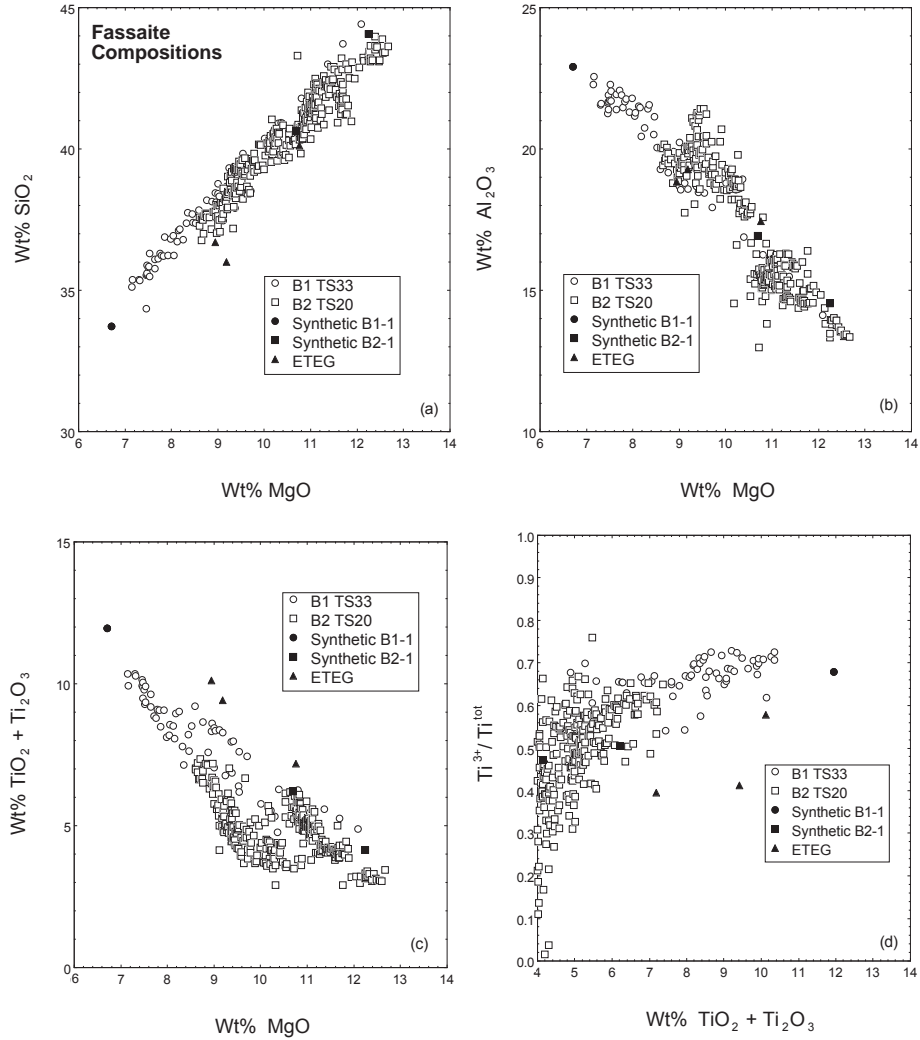
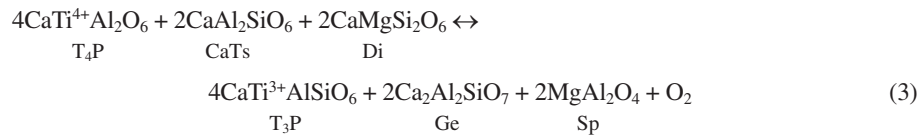


**Figure 1.** Mean compositions of fassaite crystals synthesized in each of the experiments listed in Table 1, compared to individual analyses of fassaite from two Allende inclusions. (a) SiO<sub>2</sub> vs. MgO; (b) Al<sub>2</sub>O<sub>3</sub> vs. MgO; (c) TiO<sub>2</sub> + Ti<sub>2</sub>O<sub>3</sub> vs. MgO; (d) Ti<sup>3+</sup>/Ti<sup>tot</sup> vs. TiO<sub>2</sub> + Ti<sub>2</sub>O<sub>3</sub>.

$$\ln K_1 = \ln \left[ \frac{a_{\text{T}_3\text{P}}^4 \cdot a_{\text{Ak}}^2 \cdot a_{\text{Sp}}^2 \cdot f_{\text{O}_2}}{a_{\text{T}_4\text{P}}^4 \cdot a_{\text{Di}}^4} \right] \quad (2)$$

where  $K_1$  is the equilibrium constant and  $a_i$  is the activity of component  $i$ . The second reaction is





where CaTs is the Ca-Tschermak's component of pyroxene and Ge is the gehlenite component of melilite, and for which

$$\ln K_3 = \ln \left[ \frac{a_{T_3P}^4 \cdot a_{Ge}^2 \cdot a_{Sp}^2 \cdot f_{O_2}}{a_{T_4P}^4 \cdot a_{CaTs}^2 \cdot a_{Di}^2} \right] \quad (4)$$

where  $K_3$  is the equilibrium constant.

In both the experimental run products and natural refractory inclusions, spinel is virtually pure  $MgAl_2O_4$ . Therefore, the activity of  $MgAl_2O_4$  in spinel is assumed to be one in this work. Similarly, in both the experimental run products and in natural refractory inclusions, melilite can be considered a binary solid solution of gehlenite and åkermanite, and fassaite a quaternary solid solution of all components mentioned above. The general expression relating the activity of component  $i$ ,  $a_i$ , to its concentration in such a solid solution is  $a_i = X_i \gamma_i$ , where  $X_i$  and  $\gamma_i$  are the mole fraction and activity coefficient, respectively, of component  $i$  in the solid solution. Because deviations from ideality are small in melilite (Bottinga and Richet 1978; Charlu et al. 1981), because the contributions of activities of melilite components to the  $f_{O_2}$  determination are overwhelmed by those of the pyroxene components, as seen in Equations (2) and (4), and because there is so little difference between the temperature and melilite compositions of the synthesis experiments and those of the natural assemblages to which they are applied, it is assumed here that  $\gamma_{Ge} = \gamma_{Ak} = 1$ , making  $a_{Ge} = X_{Ge}$  and  $a_{Ak} = X_{Ak}$ .

In this work, nonideal, multicomponent clinopyroxene solid solutions are treated with a Margules expansion like that given by Helffrich and Wood (1989). In this formulation, the natural logarithm of the activity coefficient of each component is the sum of a series of terms, each of which contains a binary interaction or Margules parameter,  $W_{ij}$ , defined such that  $RT \ln \gamma_j = W_{ij}$ , where  $\gamma_j$  is the activity coefficient of component  $j$  at infinite dilution in the binary  $ij$ . The Margules parameter is a function of temperature and pressure, but is independent of composition. The solution properties of the Di-CaTs join were studied by Gasparik and Lindsley (1980), who found that  $W_{CaTs,Di} = 9857 - 7.385T(K)$  and  $W_{Di,CaTs} = -2.928T(K)$  cal/mole. The interaction parameters of  $T_3P$  with all other components, and of  $T_4P$  with all other components, are unknown. Assuming that  $W_{ij} = 0$  whenever  $i$  or  $j$  are  $T_3P$  or  $T_4P$ , the following expressions can be derived:

$$RT \ln \gamma_{Di} = X_{CaTs} \left\{ W_{CaTs,Di} \left[ (1/2)(1 + X_{Di} - X_{CaTs}) + X_{Di} X_{CaTs} - X_{Di}^2 \right] + W_{Di,CaTs} \left[ (1/2)(1 + X_{CaTs} - 3X_{Di}) + X_{Di}^2 - X_{Di} X_{CaTs} \right] \right\} \quad (5)$$

and

$$RT \ln \gamma_{CaTs} = X_{Di} \left\{ W_{CaTs,Di} \left[ (1/2)(1 + X_{Di} - 3X_{CaTs}) - X_{Di} X_{CaTs} + X_{CaTs}^2 \right] + W_{Di,CaTs} \left[ (1/2)(1 + X_{CaTs} - X_{Di}) - X_{CaTs}^2 + X_{Di} X_{CaTs} \right] \right\} \quad (6)$$

After substituting for the activities, Equation (2) can be rewritten as

$$\ln K_1 = 4 \ln \left[ \frac{X_{T_3P}}{X_{T_4P} X_{Di}} \right] + 4 \ln \left[ \frac{\gamma_{T_3P}}{\gamma_{T_4P} \gamma_{Di}} \right] + 2 \ln X_{Ak} + \ln f_{O_2} \quad (7)$$

or

$$\ln K'_1 = 4 \ln \left[ \frac{X_{T_3P}}{X_{T_4P} X_{Di}} \right] - 4 \ln \gamma_{Di} + 2 \ln X_{Ak} + \ln f_{O_2} \quad (8)$$

where

$$\ln K'_1 = \ln K_1 - 4 \ln \left[ \frac{\gamma_{T_3P}}{\gamma_{T_4P}} \right] \quad (9)$$

Similarly, Equation (4) can be rewritten as

$$\ln K_3 = 4 \ln \left[ \frac{X_{T_3P}}{X_{T_4P}} \right] + 4 \ln \left[ \frac{\gamma_{T_3P}}{\gamma_{T_4P}} \right] - 2 \ln [X_{CaTs} X_{Di}] - 2 \ln [\gamma_{CaTs} \gamma_{Di}] + 2 \ln X_{Ge} + \ln f_{O_2} \quad (10)$$

or

$$\ln K'_3 = 4 \ln \left[ \frac{X_{T_3P}}{X_{T_4P}} \right] - 2 \ln [X_{CaTs} X_{Di}] - 2 \ln [\gamma_{CaTs} \gamma_{Di}] + 2 \ln X_{Ge} + \ln f_{O_2} \quad (11)$$

where

$$\ln K'_3 = \ln K_3 - 4 \ln \left[ \frac{\gamma_{T_3P}}{\gamma_{T_4P}} \right] \quad (12)$$

Using Equations (5) and (8), a value of  $\ln K'_1$  was calculated from the compositions of coexisting melilite and fassaite in each of runs 83L-37, 83L-33 and 83L-34, and the  $f_{O_2}$  at which each was produced. An analogous set of calculations was done for  $\ln K'_3$ . Results are shown in Table 6. At the  $1\sigma$  level, the data for 83L-33 and -34 are in agreement with one another but those for 83L-37 are slightly higher for  $\ln K'_1$ . Assuming that variations of  $\ln K'_1$  and  $\ln K'_3$  are insignificant over the 15 °C temperature interval over which these experiments were conducted, and that differences in fassaite composition between runs result in insignificant differences in  $\gamma_{T_3P}/\gamma_{T_4P}$  between them, means for each of  $\ln K'_1$  and  $\ln K'_3$  were obtained by weighting the three estimates of each by the inverse square of their uncertainties. Because spinel was not produced in runs 83L-17, 83L-18 or 83L-19,  $a_{Sp} < 1$  for these experiments. Inspection of Equations (2) and (4) shows that upper limits to each of  $\ln K'_1$  and  $\ln K'_3$  can be obtained from each of the latter runs by assuming that  $a_{Sp} = 1$ . These are also given in Table 6, from which it can be seen that the upper limits derived from 83L-18 and -19 are in good agreement with one another but those from 83L-17 are significantly higher, for both  $\ln K'_1$  and  $\ln K'_3$ . As a result, only the upper limit from 83L-17 is compatible with the weighted mean for each of  $\ln K'_1$  and  $\ln K'_3$ .

**Table 6.** Experimentally determined equilibrium constants for reactions (1) and (3).

Run	Bulk Composition	$\ln K'_1$	$\ln K'_3$
83L-37	B1-1	$-39.365 \pm 1.206$	$-37.500 \pm 1.171$
83L-33	B2-1	$-42.928 \pm 1.378$	$-40.490 \pm 1.358$
83L-34	B2-1	$-44.074 \pm 3.057$	$-42.672 \pm 3.059$
<b>Weighted mean</b>		<b><math>-41.168 \pm 0.870</math></b>	<b><math>-39.078 \pm 0.852</math></b>
83L-17	ETEG	$<-41.376 \pm 0.900$	$<-40.127 \pm 0.872$
83L-18	ETEG	$<-44.854 \pm 2.174$	$<-44.207 \pm 2.215$
83L-19	ETEG	$<-44.870 \pm 0.929$	$<-43.250 \pm 0.915$

Results for ETEG represent upper limits because of the absence of spinel from those runs.

### Selection of fassaite-melilite pairs

Use of the thermodynamic data obtained above to obtain an accurate estimate of the  $f_{O_2}$  at which a particular refractory inclusion formed requires determination of the compositions of melilite and fassaite grains that co-crystallized in the parent melt. The following phase equilibrium considerations influence the selection of melilite-fassaite pairs deemed to be cogenetic. In Allende and other CV3 chondrites, there are three major types of refractory inclusions that crystallized from melts, compact Type As (abbreviated CTAs), Type B1s and Type B2s. The bulk chemical compositions of all three types can be represented by projection from spinel onto the gehlenite-forsterite ( $Mg_2SiO_4$ )-anorthite plane of the  $CaO-MgO-Al_2O_3-SiO_2$  system, on which their liquid-crystal phase relations can be seen (Stolper 1982). Upon cooling liquids of these compositions at equilibrium, spinel crystallizes first at temperatures above 1500 °C, followed at ~1400 °C by melilite whose åkermanite content increases with decreasing temperature, and then anorthite followed closely by fassaite at ~1230 °C. The liquid disappears at a slightly lower temperature. The sequence of crystallization of the phases is independent of  $f_{O_2}$ , and the appearance temperatures nearly so (Stolper and Paque 1986). All three inclusion types plot in the melilite primary phase field of the plane. Because the silica content increases in the order compact Type As, Type B1s and Type B2s (Grossman et al. 2000; Simon and Grossman 2004), the compact Type As plot close to the gehlenite-forsterite axis of the plane, the Type B1s mid-way between that axis and the spinel-melilite-anorthite cotectic, and the Type B2s in a continuum from the field of the Type B1s to the cotectic. Because of this, almost all melilite crystallizes before fassaite in compact Type As, a great deal of the melilite crystallizes before fassaite in Type B1s and relatively little of the melilite crystallizes before fassaite in the Type B2s.

The compositions of all melilite-fassaite pairs used for oxygen barometry are given in Table 7. Two Allende compact Type A inclusions, TS68 and A37, both described by Simon et al. (1999), were selected for this purpose. In TS68, the edges of three different fassaite grains and their adjacent melilite were selected as three cogenetic pairs.  $X_{Åk}$  of the selected melilite ranges from 0.31 to 0.36. These compositions plot in the high-Åk tail of the melilite composition histogram for this inclusion (Simon et al. 1999), suggesting that they are among the lowest-temperature melilite grains that crystallized from its parent liquid, consistent with their being cogenetic with fassaite in inclusions of this composition. Similarly, three such pairs were selected from A37. One of the melilite compositions is Åk49, very nearly the most Åk-rich melilite in the inclusion (Simon et al. 1999), and thus nearly the last to crystallize, but the other two are Åk34 and Åk36, still quite late but significantly earlier than the former in the crystallization history.

In Type B1 inclusions, individual melilite crystals are normally zoned from early, high-temperature, Åk-poor to late, lower-temperature, Åk-rich compositions, except for portions of some crystals over which the zoning is reversed, i.e. Åk content decreasing toward the crystal exterior. This reverse zoning was reproduced experimentally by MacPherson et al. (1984b), and found to be related to the abrupt decline in the Mg/Al ratio of the coexisting liquid due to the onset of fassaite co-crystallization with melilite. Thus, for the Type B1s considered here, TS23 and TS34, the composition of the first-formed fassaite, that in the crystal cores, was taken to be cogenetic with the melilite composition at the point of reversal. For the Type B2 inclusion TS21, the melilite composition at the point of zoning reversal was found to average Åk47 for five crystals. That melilite composition was assumed to be cogenetic with the earliest fassaite to form in the inclusion. Simon et al. (1991) showed that the Ti content declines monotonically from the earliest to the latest fassaite during crystallization of Type B inclusion melts, so the average of the nine highest-Ti fassaite analyses from a total of 225 in TS21 was taken as the composition that co-crystallized with the selected melilite composition.

**Table 7.** Mean compositions of coexisting fassaite and melilite in different types of Allende refractory inclusions.

	Compact Type As		Type B1s		Type B2s	
	A37	TS68	TS23	TS34	TS21	TS20
MgO (wt%)	6.62 ± 0.16	5.73 ± 1.16	7.60 ± 0.31	7.95 ± 0.43	8.20 ± 0.19	8.85 ± 0.29
Al <sub>2</sub> O <sub>3</sub>	18.89 ± 0.60	19.94 ± 2.28	19.75 ± 0.35	19.24 ± 0.98	20.10 ± 0.22	19.65 ± 0.53
SiO <sub>2</sub>	31.71 ± 0.36	31.66 ± 2.22	34.28 ± 1.07	36.34 ± 1.00	35.82 ± 0.77	38.30 ± 0.83
CaO	24.62 ± 0.13	24.84 ± 0.21	24.78 ± 0.24	24.99 ± 0.27	24.60 ± 0.11	23.69 ± 0.12
Sc <sub>2</sub> O <sub>3</sub>	0.64 ± 0.09	<0.76	0.24 ± 0.03	0.20 ± 0.03	0.13 ± 0.04	n. d.
TiO <sub>2</sub> <sup>tot</sup>	17.93 ± 0.10	18.64 ± 1.52	10.93 ± 0.68	11.88 ± 0.54	8.24 ± 0.18	7.26 ± 0.73
V <sub>2</sub> O <sub>3</sub>	0.27 ± 0.01	0.46 ± 0.25	0.29 ± 0.04	0.53 ± 0.07	0.52 ± 0.03	n. d.
FeO	BDL	<0.08	0.03 ± 0.01	BDL	BDL	n. d.
Ti <sub>2</sub> O <sub>3</sub>	11.21 ± 0.21	13.31 ± 0.50	6.43 ± 1.09	7.86 ± 0.79	4.36 ± 0.46	4.51 ± 0.39
TiO <sub>2</sub>	5.62 ± 0.20	4.05 ± 0.87	3.94 ± 0.91	3.13 ± 0.68	3.44 ± 0.54	2.08 ± 0.59
SUM	99.57 ± 0.50	100.30 ± 0.68	97.34 ± 1.13	100.24 ± 0.54	97.18 ± 0.59	97.08 ± 0.29
<b>Cations in Formula with 4 Total Cations, including 1 Ca Cation, per 6 Oxygen Anions</b>						
Si	1.218 ± 0.015	1.213 ± 0.091	1.326 ± 0.025	1.355 ± 0.033	1.370 ± 0.016	1.434 ± 0.030
<sup>IV</sup> Al	0.782 ± 0.015	0.787 ± 0.091	0.674 ± 0.025	0.645 ± 0.033	0.630 ± 0.016	0.566 ± 0.030
<sup>VI</sup> Al	0.073 ± 0.009	0.112 ± 0.014	0.226 ± 0.012	0.203 ± 0.016	0.276 ± 0.006	0.301 ± 0.006
Mg	0.379 ± 0.010	0.327 ± 0.068	0.438 ± 0.018	0.443 ± 0.022	0.468 ± 0.009	0.494 ± 0.015
Fe	0	<0.002	0.001 ± 0.000	0	0	–
Sc	0.022 ± 0.003	<0.026	0.008 ± 0.001	0.006 ± 0.001	0.004 ± 0.001	–
V	0.008 ± 0.000	0.013 ± 0.007	0.008 ± 0.001	0.015 ± 0.002	0.015 ± 0.001	–
Ti <sup>3+</sup>	0.357 ± 0.008	0.421 ± 0.016	0.205 ± 0.034	0.245 ± 0.025	0.138 ± 0.014	0.145 ± 0.013
Ti <sup>4+</sup>	0.161 ± 0.005	0.116 ± 0.025	0.113 ± 0.027	0.088 ± 0.019	0.099 ± 0.016	0.060 ± 0.017
Ti <sup>3+</sup> /Ti <sup>4+</sup>	2.218 ± 0.118	3.737 ± 0.627	1.935 ± 0.674	2.991 ± 1.001	1.451 ± 0.337	2.553 ± 0.686
<b>Mole Fractions of Pyroxene Components</b>						
Di	0.387 ± 0.007	0.334 ± 0.063	0.446 ± 0.018	0.452 ± 0.022	0.477 ± 0.008	0.494 ± 0.015
CaTs	0.084 ± 0.013	0.115 ± 0.016	0.230 ± 0.012	0.207 ± 0.016	0.281 ± 0.007	0.301 ± 0.006
T <sub>3</sub> P	0.364 ± 0.007	0.432 ± 0.026	0.208 ± 0.035	0.252 ± 0.027	0.141 ± 0.015	0.145 ± 0.013
T <sub>4</sub> P	0.165 ± 0.008	0.119 ± 0.028	0.115 ± 0.028	0.089 ± 0.019	0.101 ± 0.016	0.060 ± 0.017
# analyses	3	3	7	34	9	5
<b>Melilite</b>						
X <sub>Ak</sub>	0.397 ± 0.082	0.340 ± 0.027	0.666 ± 0.0024	0.653 ± 0.0024	0.469 ± 0.031	0.466 ± 0.014
# analyses	3	3	3	6	5	5

n. d.: not determined. BDL: below detection limit of electron probe, 0.03 wt% FeO. Uncertainties are one standard deviation; upper limits are 2σ.

For the Type B2 inclusion TS20, reverse zoning of the melilite is not observed, so the average composition of the outer 20 μm of a fassaite grain and the outer 20 μm of a nearby melilite grain were assumed to be a cogenetic pair. Care must be exercised when adopting the latter approach in the case of Type B2 inclusions because the fassaite in these objects is commonly sector-zoned, with the edge of a grain parallel to one crystal face having a significantly higher  $X_{\text{CaTs}}/X_{\text{Di}}$  ratio and slightly higher  $X_{\text{T3P}}/X_{\text{T4P}}$  ratio than the edge of the same grain parallel to an intersecting crystal face (Simon and Grossman 2006).

### Oxygen barometry

**Types A and B refractory inclusions.** In order to determine the  $f_{O_2}$  of the gas in equilibrium with the liquid from which each of the above refractory inclusions crystallized, the fassaite composition from each fassaite-melilite pair in Table 7 was used to calculate  $\gamma_{Di}$  from Equation (5), which was then substituted into Equation (8), together with the compositions of both phases and the weighted mean value of  $\ln K'_1$  from Table 6. A separate estimate of the  $f_{O_2}$  for each inclusion was obtained in an analogous calculation using the weighted mean value of  $\ln K'_3$  from Table 6 in Equation (11). Results are shown in Table 8. In estimating the  $f_{O_2}$  in this way, it is assumed that differences in fassaite crystallization temperatures and in  $\gamma_{T,P}/\gamma_{T,P}$  ratios that may exist between the natural samples and synthetic analogs produce insignificant differences in the values of  $\ln K'_1$  and  $\ln K'_3$ . It should be noted, however, that fassaite in natural inclusions may have crystallized at temperatures significantly below those where fassaite formed in isothermal experiments. Stolper and Paque (1986) reviewed evidence that Type B inclusions experienced maximum temperatures of  $\sim 1673$  K and cooling rates of several tens of degrees per hour and presented experimental data that show that, under these conditions, the temperature of fassaite appearance may be depressed by up to 50–70 K relative to its equilibrium crystallization temperature. Because the temperature dependences of  $\ln K'_1$  and  $\ln K'_3$  are not known, there may be a significant error in estimating the  $f_{O_2}$  of crystallization of natural inclusions from these experimental results.

For every inclusion, the  $\log f_{O_2}$  determined from Equation (1) is within  $1\sigma$  of that from Equation (3). Also, the  $\log f_{O_2}$  determined for each inclusion is always within  $1\sigma$  of that for the other inclusion of the same type. For the Type B2 inclusion TS20, substitution of the mean composition of the edge of the fassaite grain in one sector with that in the other sector gives rise to a change of 0.1 in  $\log f_{O_2}$ . For each of Equations (1) and (3), the range of values of  $\log f_{O_2}$  overlap for all inclusion types within  $1\sigma$ , except that the CTA range lies slightly outside the range for Type B2s in the case of Equation (3).

Grossman et al. (2000) showed that the departures of major element compositions of refractory inclusions from those of calculated high-temperature condensate assemblages are consistent with the magnitudes of evaporative losses of magnesium and silicon inferred from the heavy isotope enrichments of these elements in bulk inclusions. Evaporation occurred while these objects were at least partially molten (Davis et al. 1990) and constitutes direct evidence that the MgO and SiO<sub>2</sub> contents of these liquids were not in equilibrium with the surrounding gas. If lack of equilibrium persisted to the relatively low temperature at which fassaite crystallized from the liquid, fassaite crystallization would have occurred during a continuous change in bulk composition. Under such open-system conditions, there would be no guarantee that the internal  $f_{O_2}$  of the droplet recorded by the Ti<sup>3+</sup>/Ti<sup>4+</sup> ratio of the fassaite was the same as that of the surrounding gas. Nevertheless, core-to-rim traverses of fassaite crystals in Type B2 inclusions show that the Ti<sup>3+</sup>/Ti<sup>4+</sup> ratio did not vary during the entire

**Table 8.** Oxygen fugacities calculated for natural refractory inclusions.

Inclusion	Type	$\log f_{O_2}$ , reaction 1	$\log f_{O_2}$ , reaction 3
A37	CTA	$-19.924 \pm 0.438$	$-20.437 \pm 0.423$
TS68	CTA	$-20.910 \pm 0.666$	$-21.236 \pm 0.601$
TS23	B1	$-19.782 \pm 0.649$	$-18.581 \pm 0.639$
TS34	B1	$-20.520 \pm 0.575$	$-19.473 \pm 0.564$
TS21	B2	$-18.911 \pm 0.514$	$-18.302 \pm 0.384$
TS20	B2	$-19.797 \pm 0.651$	$-19.169 \pm 0.640$
<b>Average</b>		<b><math>-19.974 \pm 0.689</math></b>	<b><math>-19.533 \pm 1.120</math></b>

interval of fassaite crystallization (Simon and Grossman 2006), indicating that open-system behavior had ceased by this stage, presumably because the droplets had equilibrated their  $f_{\text{O}_2}$  with the surrounding gas. In contrast, on the basis of core-to-rim zonation of the  $\text{Ti}^{3+}/\text{Ti}^{4+}$  ratio within individual fassaite crystals in Type B1 inclusions, Simon et al. (1991) suggested that, as fassaite crystallization from Type B1 droplets proceeded, its composition departed progressively from that which would have been in equilibrium with the gas. According to this view, only the cores of fassaite crystals in Type B1s equilibrated with the gas, and the fact that the core compositions selected for the present work record the same  $f_{\text{O}_2}$  as the other inclusion types suggests that this is indeed the case.

The best estimate for  $\log f_{\text{O}_2}$  of the gas in equilibrium with the liquid from which each melilite-pyroxene pair crystallized, is obtained by averaging together all 12 results given in Table 8. The value so obtained,  $-19.8 \pm 0.9$ , is plotted in Figure 2, assuming that fassaite in all of these inclusions crystallized at the average temperature of the three experiments, 1509 K. Further evidence that these phases formed at very low  $f_{\text{O}_2}$  comes from the valence of V in the fassaite. Using XANES spectroscopy, S. Simon et al. (2005) determined that the fassaite in two of the samples in Table 8, TS34 and TS21, contains approximately equal amounts of  $\text{V}^{2+}$  and  $\text{V}^{3+}$ . In a V-doped CMAS glass synthesized at  $f_{\text{O}_2} = 10^{-18}$  and 1583 K, Sutton et al. (2005) also found that a large proportion of the V,  $\sim 25\%$ , is  $\text{V}^{2+}$ . The formation conditions of the glass are not very far from those inferred for the fassaite in Table 8.

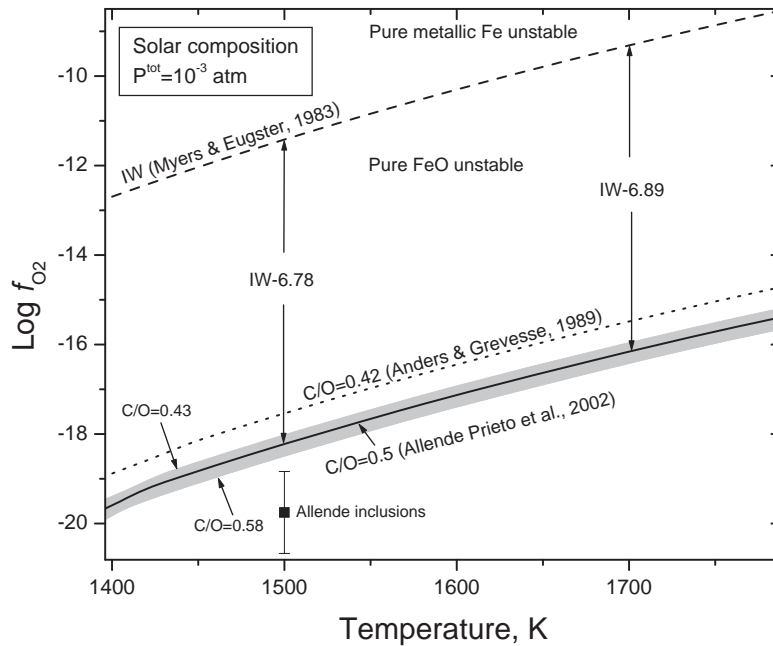


**Figure 2.** Variation of the logarithm of the equilibrium  $f_{\text{O}_2}$  with temperature in a system of solar composition undergoing condensation at a  $P^{\text{tot}}$  of  $10^{-3}$  atm for two different estimates of the solar C/O ratio, including the preferred value of 0.5 (Allende Prieto et al. 2002). The iron-wüstite buffer curve, IW, is shown for reference, from which it is seen that the curve for solar composition lies 6.8 to 6.9 log units below the condition for equilibrium between metallic iron and pure FeO in the temperature interval 1500 K to 1700 K at this  $P^{\text{tot}}$ . Shown also is the value of the  $\log f_{\text{O}_2}$  of the gas in equilibrium with the liquid from which melilite and fassaite co-crystallized in Allende Types A and B refractory inclusions, as determined experimentally in this work.

Also plotted in Figure 2 is the temperature variation of the logarithm of the equilibrium  $f_{O_2}$  in a system of solar composition undergoing condensation at a  $P^{tot}$  of  $10^{-3}$  atm for two different estimates of the solar C/O ratio, 0.42 (Anders and Grevesse 1989) and the preferred value of 0.50 (Allende Prieto et al. 2002). Unless otherwise stated, all condensation calculations performed for the present work employ the same computer program, sources of thermodynamic data and Solar System elemental abundances as in Fedkin and Grossman (2006). In Figure 2, the shaded region about the curve for the preferred value of the solar C/O ratio was obtained from condensation calculations performed at two different C/O ratios, 0.432 and 0.581, obtained by propagating the errors quoted by Allende Prieto et al. (2001) for oxygen and Allende Prieto et al. (2002) for carbon. At 1509 K, a system of solar composition has  $\log f_{O_2} = -18.1^{+0.2}_{-0.3}$ .

If fassaite in compact Type A, Type B1 and Type B2 inclusions in the Allende meteorite crystallized at 1509 K, they did so at an  $f_{O_2}$  1.6 log units below that of a system of solar composition. Considering the  $1\sigma$  error bounds on both values,  $\log f_{O_2}$  for the refractory inclusions could be as high as -18.8 and that for solar composition at the same temperature could be as low as -18.4, a difference of only a factor of 2.5 in  $f_{O_2}$ . It is conceivable that real differences in the  $\gamma_{Ti^{3+}}/\gamma_{Ti^{4+}}$  ratios between the synthetic and natural fassaite, assumed negligible in this treatment, could be large enough to make up this difference. Similarly, the difference could also be made up if crystallization of the meteoritic fassaite occurred at a temperature 40 K below its equilibrium crystallization temperature, a very real possibility in view of the cooling rate study of Stolper and Paque (1986), assuming that  $\ln K'_1$  and  $\ln K'_3$  vary insignificantly over this temperature interval. If the value of the C/O ratio for solar composition were  $\sim 0.69$ , or 38% larger than that measured by Allende Prieto et al. (2002), the  $f_{O_2}$  of solar gas would be in minimal agreement with that indicated by refractory inclusions.

All in all, the  $Ti^{3+}/Ti^{4+}$  ratio of fassaite in Allende inclusions implies that they equilibrated in a system whose  $f_{O_2}$  was quite close to that of a system of solar composition. As will be seen in the remainder of this paper, this is the only oxygen fugacity indicator that implies that any object in chondrites formed in a system that was near-solar in composition.

**Constraints from siderophile elements.** In contrast to the very low  $f_{O_2}$  indicated by the  $Ti^{3+}/Ti^{4+}$  ratio of their fassaite, a much higher  $f_{O_2}$  has been inferred for formation of some Types A and B inclusions in CV3 chondrites on the basis of the relative abundances in them of refractory siderophile elements such as Os, Ir, Ru, Pt, W, Mo, etc. Within the inclusions, a large fraction of each of these elements is known to reside in 1-1000  $\mu m$  aggregates of metallic, oxide and sulfide phases, called Fremdlinge (El Goresy et al. 1978) or opaque assemblages (Blum et al. 1989). In the case of most refractory inclusions, when the concentration of each refractory siderophile element is normalized to its abundance in C1 chondrites, a uniform enrichment factor is found (Grossman et al. 1977). Fegley and Palme (1985) reported a group of nine objects, however, in which the enrichment factors for Mo are more than 25% below those for Os; of those, four have enrichment factors for W which are also more than 25% below those for Os. These workers also used thermodynamic calculations to show that refractory metal alloys with W and Mo depletions of this minimum size are a natural consequence of condensation in a system whose  $P_{H_2O}/P_{H_2}$  ratio is  $>10^{-2}$  but which is otherwise solar in composition, and proposed such an environment of formation for the metallic component of each inclusion. At refractory siderophile element condensation temperatures, the minimum  $\log f_{O_2}$  corresponding to this ratio is  $\sim$ four log units below that for iron-wüstite equilibrium, abbreviated IW-4 in this work, and  $\sim$ three log units higher than that of a system of solar composition. Two of the four samples, however, are themselves Fremdlinge, not whole inclusions. Palme et al. (1994) showed convincing observational evidence for removal of W and Mo from Fremdlinge and deposition of those elements in the adjacent silicates of the host inclusion. They further reported experimental evidence for mobilization of these elements at an  $f_{O_2} \sim 11$  log units higher than in a system of solar composition, suggesting that the process occurred during parent



body metamorphism. Under these circumstances, convincing evidence for condensation under oxidizing conditions would have to come from refractory siderophile abundances in whole inclusions, assuming that the latter were not modified by reaction with surrounding matrix. Although the remaining two samples that show both W and Mo depletions are whole inclusions, one of them belongs to a peculiar class of objects called FUN inclusions. Unlike normal refractory inclusions, these objects possess unique nuclear isotope anomalies as well as extreme isotopic mass-fractionations in relatively refractory lithophile elements, and some have large depletions of Ce relative to La compared to solar abundances. The latter feature requires condensation at an  $f_{O_2}$  at least several log units higher than at the same temperature in a system of solar composition, possibly within supernova ejecta (Davis et al. 1982). Thus, while this object may have formed under oxidizing conditions, there is no evidence that its origin is applicable to most refractory inclusions. The idea that condensation of the metallic part of normal Types A and B inclusions occurred under much more oxidizing conditions than are possible in a system of solar composition is thus based on analysis of part of a single inclusion, and must therefore be considered as speculative at this point.

**Implications for the X-wind model.** As pointed out by Wood (2004), the very low  $f_{O_2}$  under which Types A and B inclusions formed argues against the X-wind model, an idea proposed by Shu et al. (2001) in which these objects formed by repeated evaporation and condensation due to solar flares in a reconnection region close to the protosun. Based on Shu et al.'s model calculations, S. Desch (pers comm) calculated that such an environment would have had a mass ratio of evaporated dust to residual gas of  $\sim 120$ . For anhydrous dust of OC composition (see below), this is equivalent to a dust/gas enrichment factor of  $\sim 25,000$  relative to solar composition, yielding an atomic O/H ratio of  $\sim 3.4$ , or nearly  $6 \times 10^3$  times that of solar composition. In condensation calculations in a system of this composition at an appropriately low  $P^{tot}$  of  $\sim 3 \times 10^{-11}$  atm, Ca-rich clinopyroxene becomes stable at  $\sim 1415$  K where  $\log f_{O_2} \sim IW + 1$ ,  $\sim 7.8$  log units higher than that of a solar gas, and totally inconsistent with the  $Ti^{3+}/Ti^{4+}$  ratio of fassaite in refractory inclusions. It might be argued that chemical equilibrium would not be achieved in such an environment of repeated high-energy ionization events. The observations, however, are that all compact Type A inclusions have the same mineral assemblage as one another, as do all Type B inclusions, including fassaite with similar  $Ti^{3+}/Ti^{4+}$  ratio, and they just happen to be mineral assemblages that would crystallize from liquids in chemical equilibrium with a gas whose  $f_{O_2}$  is very close to that expected in a system of solar composition at their solidification temperatures.

**$f_{O_2}$  of formation of Wark-Lovering rims.** Types A and B inclusions are each surrounded by a sequence of very narrow, monomineralic rim layers (Wark and Lovering 1977). At the outermost reaches of all inclusions, these so-called Wark-Lovering rims are each 5 to 20  $\mu m$  wide and are found in a nearly constant mineralogical sequence. Progressing from the interior to the exterior of each inclusion, the most common sequence of layers consists of spinel + perovskite, then melilite, then clinopyroxene ranging in composition outward from Ti-, Al-rich fassaite to relatively low-Ti and low-Al diopside, and finally hedenbergite + andradite ( $Ca_3Fe_2Si_3O_{12}$ ). The innermost layers are thought to have formed simultaneously by reaction with nebular gas during the last stages of CAI formation (MacPherson et al 1981) but the outermost layer of hedenbergite, containing  $Fe^{2+}$ , and andradite, containing  $Fe^{3+}$ , probably formed after the other rim layers, by metamorphism in the parent bodies of the inclusions (MacPherson and Krot 2002). An alternative view, that the innermost rim layers formed by flash heating-induced volatilization of the outer few hundred  $\mu m$  of the inclusions followed by reaction with an external source of Mg and Si, has been argued by Ruzicka (1997) and Wark and Boynton (2001).

J. Simon et al. (2005) analyzed fassaite in the Wark-Lovering rim of a compact Type A inclusion from Leoville by electron microprobe. Applying a stoichiometric assumption similar to that used here and described above to extract the  $Ti^{3+}/Ti^{4+}$  ratio from their analytical data, they found no evidence for  $Ti^{3+}$ , and argued from this that the  $f_{O_2}$  of the solar nebula was  $\sim 6$

log units higher when the rims formed than when the interior fassaite formed. When S. Simon et al. (2007) used an electron microprobe to analyze fassaite in the rim of a fluffy Type A inclusion from Allende, they also found fassaite with  $\text{Ti}^{3+}/\text{Ti}^{4+}$  ratios that are either zero or very low where the fassaite was immediately adjacent to the contact of the pyroxene layer with the inner spinel layer, but in addition, they found that the  $\text{Ti}^{3+}/\text{Ti}^{4+}$  ratios increase with distance from the contact, reaching values like those of fassaite in inclusion interiors. Furthermore, when S. Simon et al. (2007) measured the  $\text{Ti}^{3+}/\text{Ti}^{4+}$  ratio directly by XANES spectroscopy along a traverse across the same fassaite layer, all  $\text{Ti}^{3+}/\text{Ti}^{4+}$  ratios were found to be within the normal range of those of interior fassaite. According to the stoichiometric method, when all Ti is calculated as  $\text{Ti}^{4+}$ , the further the resulting total cation/oxygen ratio is below 0.66, the greater the proportion of the Ti that is trivalent. The discrepancy between electron microprobe and spectroscopic data is probably the result of inclusion of small amounts of phases with cation/oxygen ratios that are higher than 0.66, such as spinel (0.75), within the analytical volume, a possibility which always exists but which is exacerbated in this case by the relatively low  $\text{TiO}_2^{\text{tot}}$  (<6 wt%) and small grain size of the rim fassaite. S. Simon et al. (2007) concluded that affected analyses were probably included by J. Simon et al. (2005) in their calculation of the average rim pyroxene composition, causing underestimation of the  $\text{Ti}^{3+}/\text{Ti}^{4+}$  ratio of rim pyroxene in the J. Simon et al. (2005) work. There is thus no basis for concluding that the rims on inclusions formed at a higher  $f_{\text{O}_2}$  than the interiors.

***$f_{\text{O}_2}$  of formation of refractory inclusions in CM2 chondrites.*** Refractory inclusions in Murchison and other CM2 chondrites are mineralogically quite distinct from the Types A and B inclusions in CV3 chondrites, discussed above. Most of the refractory inclusions in the CM2 chondrites are hibonite ( $\text{CaAl}_{12}\text{O}_{19}$ )- and spinel-rich and contain very little  $\text{SiO}_2$  (MacPherson et al. 1983). Because of this, they are thought to have sampled higher-temperature condensates than those in CV3 chondrites (MacPherson et al. 1984a). Of the two phases used above for oxygen barometry, melilite is rare and fassaite extremely rare in the CM2 inclusions. Nevertheless, Ihinger and Stolper (1986) used optical spectroscopy to show that blue hibonite from the Murchison inclusion Blue Angel contains  $\text{Ti}^{3+}$ , and found that hibonite of that composition is blue when synthesized at 1430 °C over a range of  $\log f_{\text{O}_2}$  from  $-10.7$  to  $-15.0$ , the latter just 1.1 log units higher than that of a system of solar composition at the same temperature. Furthermore, electron spin resonance was used by Beckett et al. (1988) to determine that blue hibonite from the Murchison inclusion SH-7 contains 0.35 wt%  $\text{Ti}^{3+}$ , representing 23% of the total titanium in this phase. Although the presence of significant  $\text{Ti}^{3+}$  suggests that these hibonite samples formed under very reducing conditions, possibly as reducing as in a system of solar composition, quantitative estimation of the equilibrium  $f_{\text{O}_2}$  under which they formed requires precise spectrometric comparison of synthetic hibonite with the Blue Angel material and knowledge of the fraction of the  $\text{Ti}^{4+}$  that is in the 5-fold crystallographic site in the case of the SH-7 material.

## THE OXIDATION STATE OF IRON IN ORDINARY CHONDRITES

### The problem

Olivine  $[(\text{Mg,Fe})_2\text{SiO}_4]$  in primitive Solar System matter contains significant amounts of fayalite ( $\text{Fe}_2\text{SiO}_4$ ). The mean mole fraction of fayalite,  $X_{\text{Fa}}$ , in olivine is 0.05 to 0.10 in CI and CM chondrites,  $\sim 0.07$  in chondrules of CV chondrites, 0.38 in R chondrites,  $\sim 0.50$  in the matrices of CO and CV chondrites (Brearley and Jones 1998), and  $\sim 0.10$  in interplanetary dust particles (Rietmeijer 1998). Indeed, the FeO content of olivine is used to classify chondrules into two groups: Type I, or low-FeO, and Type II, or high-FeO (Scott and Taylor 1983). The division between the two groups is set at a mean molar  $\text{FeO}/(\text{FeO} + \text{MgO})$  ratio of 0.10 for olivine and low-Ca pyroxene. This division is somewhat arbitrary, as chondrules in most

primitive chondrites exhibit a very wide and continuous range of mean  $\text{FeO}/(\text{FeO} + \text{MgO})$  ratios which straddles this value. Huss et al. (1981) showed that the mean  $X_{\text{Fa}}$  of submicron olivine grains in the opaque matrix of a given type 3 unequilibrated ordinary chondrite (UOC) is systematically higher than that of the larger olivine grains inside chondrules in the same meteorite. Alexander et al. (1989) suggested that the matrix olivine grains may have formed during parent body metamorphic processes under relatively oxidizing conditions. Within the type 3 UOCs, McCoy et al. (1991) noted a progressive increase in mean  $X_{\text{Fa}}$  of olivine grains inside chondrules with increasing metamorphic grade, and attributed this to reactions between phases in chondrules and matrices during metamorphism. Grossman and Brearley (2005) found that, during incipient metamorphism of carbonaceous and ordinary chondrites, Cr, alkalis and FeS became mobile before the onset of significant modification of the histogram of fayalite contents of coarse olivine grains. In the coarsest olivine in chondrules from the three least metamorphosed ordinary chondrites which they studied, the average  $X_{\text{Fa}}$  is 0.15. While  $X_{\text{Fa}}$  of matrix olivine grains may have been altered during metamorphism, this value is probably pre-metamorphic.

The problem is how to make olivine of this composition in the solar nebula. As an initial working hypothesis, we will assume that  $\text{FeO}/(\text{FeO} + \text{MgO})$  ratios did not undergo significant change during chondrule formation. In this case, the problem becomes how to make olivine in the precursors of chondrules in ordinary chondrites with a mean  $X_{\text{Fa}}$  of 0.15. The alternative working hypothesis, that  $\text{FeO}/(\text{FeO} + \text{MgO})$  ratios did change during chondrule formation, is explored later. In both cases, the problem stems from the very reducing nature of solar gas.

During equilibrium condensation from a system of solar composition at  $P^{\text{tot}}$  between  $10^{-5}$  and  $10^{-3}$  bar, iron begins to condense as a metallic nickel-iron alloy between 35 and 75 K below the temperature at which Ca is totally condensed into refractory assemblages. During cooling in this pressure range, the magnesian end-member of the olivine solid solution series, forsterite ( $\text{Mg}_2\text{SiO}_4$ ), condenses within the next 50 K and the remainder of the Mg and Si condense as enstatite ( $\text{MgSiO}_3$ ) within the following 50-100 K. Under these conditions, the FeO content of the olivine is vanishingly small, a natural consequence of the very reducing nature of solar gas at such high temperatures. The first form of oxidized iron to become stable in a cooling gas of solar composition is fayalite. Solar gas becomes sufficiently oxidized to stabilize significant amounts of this component of olivine only at temperatures below ~800 K, several hundred degrees lower than the initial condensation temperature of forsterite. At these temperatures, since all of the Mg and Si are already condensed, the overall reaction for fayalite formation can be written as



At equilibrium, all olivine must have the same  $X_{\text{Fa}}$ , requiring diffusion of  $\text{Fe}^{2+}$  into previously formed crystals of forsterite. The Fe-Mg interdiffusion rate in olivine at  $T < 800$  K is so small, however, that insignificant amounts of FeO can be stabilized as fayalitic olivine unless the cooling time is prohibitively long,  $\gg 10^6$  yr, and/or the olivine condensate grain radius is very small,  $\ll 1 \mu\text{m}$  (Fedkin and Grossman 2006). If chondrule precursors were made of such condensate material, chondrule olivine would contain vanishingly small amounts of FeO unless the  $\text{FeO}/(\text{FeO} + \text{MgO})$  ratio of chondrules changed during melting. In this case, however, solar gas is too reducing to stabilize the required high FeO contents at melting temperatures.

The traditional way out of this long-standing problem, as reviewed by Palme and Fegley (1990) and Krot et al. (2000), is to relax the constraint that condensation took place in a gas of solar composition. In particular, if the  $f_{\text{O}_2}$  of a nebular region were enhanced sufficiently relative to that of a gas of solar composition, stabilization of oxidized iron would have occurred at a much higher temperature. Under these conditions, the diffusion rate could have been high enough to allow formation of chondrule precursor olivine with relatively high oxidized iron contents, or oxidation of iron could have occurred during chondrule melting. Two mechanisms

have been proposed for enhancing the  $f_{\text{O}_2}$  of nebular regions, enrichment in the  $P_{\text{H}_2\text{O}}/P_{\text{H}_2}$  ratio relative to solar gas by radial transport of icy planetesimals into the inner part of the nebula; and enrichment in pre-existing dust relative to gas by dust coagulation and vertical settling toward the nebular midplane. The forces driving these processes and how they work to increase the  $f_{\text{O}_2}$  are discussed in the following sections.

### Radial transport processes

Astronomical observations of young solar-mass stars have shown that these objects accrete mass through their accretionary (protoplanetary or protostellar) disks for periods of up to tens of millions of years (Calvet et al. 2005). The physical properties of the accretionary disks evolve throughout the time that they are losing mass to their central stars. As these disks serve as analogs to our own solar nebula, this means that the properties of the solar nebula, too, evolved for at least part of the time that chondritic materials were being formed.

The process (or processes) responsible for driving disk evolution is still a subject of ongoing research. Evolutionary models often assign a viscosity to the disk that is responsible for generating shear stresses between two adjacent annuli in the disk as they orbit the central star at slightly different rates (the orbital velocity falls off as  $r^{-1/2}$ ). Because the outer annulus orbits at a lower velocity, the shear stress causes the gas in the inner annulus to slow down, losing angular momentum, and therefore move inwards. Similarly, the gas in the outer annulus is “sped up” due to the stresses, increasing its angular momentum, and migrates outwards, away from the star. Thus, while the net movement of material is inward through the disk, a small amount of material diffuses outward to conserve angular momentum, causing the disk to grow in radial extent. Possible sources of viscosity in disks include magneto-rotational instabilities (MRI) (Balbus and Hawley 1991), large scale convection (Lin and Papaloizou 1980), shear instabilities (Dubrulle et al. 2005), or gravitational instabilities (Goldreich and Lynden-Bell 1965; Boss 1998; Gammie 2001).

The material transported through the solar nebular disk was predominantly hydrogen and helium gas, as those elements made up approximately 99% of the mass of material in the disk. Other vapor species were transported in the disk by the same processes, being subjected to both the large-scale flows and diffusion that operated to redistribute materials in the disk. Thus, in the absence of any sources or sinks, vapor species did not fractionate from one another as mass was redistributed in the accretionary disk.

Evolutionary models show that solids can be redistributed by a variety of processes, with each process varying in intensity depending on the size of the solid body. Small particles, defined as those whose radius,  $a$ ,  $< \sim 1$  cm, generally follow the motions of the gas and are effectively redistributed within the disk in the same manner as the vapor, being pushed about by the advective flows associated with disk evolution and diffusing along concentration gradients. Large particles ( $a > \sim 1$  km) tend to be so massive that they are unaffected by the presence of the gas, and thus follow their own orbits around the central star, being relatively immobile in terms of radial transport in the disk. Intermediate sized bodies ( $\sim 1$  cm  $< a < \sim 1$  km) experience minor transport due to advection and diffusion; however, these objects are more strongly affected by gas-drag migration. Gas-drag-induced migration arises from the fact that the gas in a protoplanetary disk is partially supported by an outward pressure gradient. This reduces the central force that the gas experiences, and thus allows it to orbit the star at a less than Keplerian rate. Solids are subjected only to the gravitational force of the star, and thus attempt to follow Keplerian orbits. This difference in orbital velocity results in the solids experiencing a headwind as they move through the gas. Thus, they lose energy and momentum and migrate inward over time. Gas-drag migration of solids can be quite rapid, with meter-sized bodies drifting inward at rates near 1 AU/100 yr. Because larger solid bodies decouple from the gas and follow their own evolutionary paths, the solid-to-gas mass ratio is expected to vary with both time and location in a protoplanetary disk. Because these bodies encounter conditions at which

water ice can volatilize, this transport process may lead to spatial and temporal fluctuations in the water vapor abundance relative to other gas species present in the disk.

Ciesla and Cuzzi (2006) recently investigated how the distribution of water was shaped by the dynamical behavior of ice and vapor in an evolving protoplanetary disk. In this work, water was considered to exist as four different species to characterize the range of dynamical behaviors expected: vapor; dust (particles with  $a < \sim 1$  cm); migrators ( $\sim 1$  cm  $< a < \sim 1$  km); and planetesimals ( $a > \sim 1$  km), with each of these species being subjected to transport by the processes described above. In addition, mass was exchanged between these species by coagulation, accretion, collisional destruction, vaporization, and condensation. A number of hypothetical protoplanetary disks were investigated, along with a range of evolutionary parameters, to identify the various water-to-hydrogen ratios that might have existed in a disk and the timescales associated with the observed variations.

While the specific results for a protoplanetary disk were found to be very sensitive to the particular parameters selected, the water distribution followed broadly similar evolutionary paths in all cases considered. During the early stages of disk evolution, small icy particles coagulated together in the outer disk to form migrators—the centimeter to tens-of-meters-sized bodies that were strongly affected by gas drag. Due to their rapid transport, these objects were able to move through the disk and reach the warm inner region inside of the snow line, where they began to vaporize. Initially, this led to water vapor being injected into the inner disk at a more rapid rate than it was removed by advection and diffusion. As a result, the concentration of water vapor relative to hydrogen increased in the inner disk, only immediately inside the snow line at first, but over time water vapor became uniformly distributed throughout the inner disk, allowing the entire inner disk to reach higher-than-canonical ratios of water to hydrogen (Fig. 3).

As dust continued to coagulate in the outer disk, the production rate of migrators declined over time as the raw material available to build these objects was depleted. In addition, the density of planetesimals in the outer disk increased over time, and these objects tended to accrete any migrators that were present rather than allow them to reach the inner disk. Meanwhile, water vapor in the inner disk diffused outward beyond the snow line, where it condensed to form water ice which was then incorporated into the local planetesimals. Eventually this removal rate exceeded the rate at which the water vapor was being resupplied, and the concentration of water vapor began to decline. Not only did the water-to-hydrogen ratio fall to the initial value for the disk, but also, since water vapor removal continued for the rest of the lifetime of the disk, the water-to-hydrogen ratio became depleted relative to the canonical ratio over time.

The level to which water was enhanced in the inner disk was sensitive to the structure of the protoplanetary disk as well as the viscosity of the disk. Ciesla and Cuzzi (2006) found, however, that the maximum enhancement the inner disk experienced was on the order of a factor of 10, though a factor of a few was more typical. While Cuzzi and Zahnle (2004) suggested that enhancements of 100 to 1000 are possible, that work considered only a steady-state case. Ciesla and Cuzzi (2006) found that reaching such high levels is nearly impossible due to the fact that there was a finite supply of ice that could be transported inward through the disk. In this model, the period of time during which the concentration of water was enhanced depended on the disk viscosity and the rate at which solids grew in the outer disk, but ranged from a few hundred thousand years to a few million.

### Vertical transport processes

Just as the radial distribution of solids is likely to deviate from that of the gas in a protoplanetary disk, so too is the vertical distribution of solids. At a particular location in a disk, a small component of the gravity from the central star pulls an object downward toward the midplane of the disk. The gas in the disk quickly reaches a state of hydrostatic equilibrium where the pressure of the gas supports the gas against the gravitational force. Solids, however,

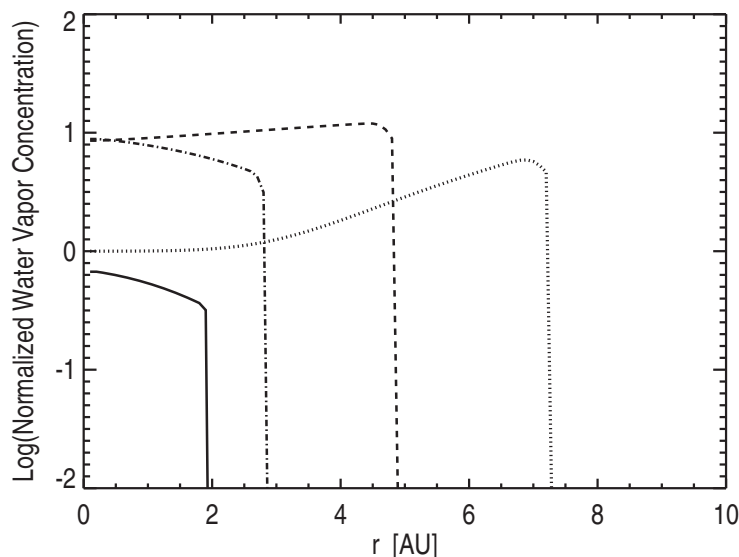


**Figure 3.** The logarithm of the calculated ratio of the total amount of water, augmented by evaporation of ice from radial migrators, to the initial amount present as a function of radial distance from the center of the model protoplanetary disk, after  $10^5$  (dotted),  $10^6$  (dashed),  $2 \times 10^6$  (dot-dashed) and  $3 \times 10^6$  yr (solid), as found by Ciesla and Cuzzi (2006). The inner disk initially is enhanced in its water vapor concentration by the inward migration of icy solids from beyond the snow line. Over time, the outer disk is depleted of water ice, leading to the eventual removal of water vapor in the inner disk by advection and diffusion. The cooling of the disk can be seen as the snow line moves inward over time (from 7 to 2 AU for the case shown).

are not supported against gravity by the pressure of the gas, and therefore continuously fall through the gas toward the disk midplane. As a solid particle settles through the gas, it feels some resistance to its motion due to drag from the gas. How strongly the solid particle is affected by this resistance can be quantified by the *stopping time*,  $t_s$ , which is given by

$$t_s = a \rho / \rho_g c, \quad (14)$$

where  $\rho$  is the mass density of the particle,  $c$  is the local speed of sound, and  $\rho_g$  is the local gas density of the nebula. This expression is valid for particles whose radius is less than the mean free path of the nebular gas, which was likely near  $\sim 50$  cm in the chondrite formation region of the solar nebula. Those particles with short stopping times ( $t_s \ll 1$  s) are strongly affected by the gas while those with larger stopping times feel negligible resistance as they settle to the disk midplane. The settling velocity of a given particle is given to be approximately  $\Omega_K^2 z t_s$ , where  $\Omega_K$  is the Keplerian rotation rate of the disk and  $z$  is the height above the midplane (Dubrulle et al. 1995).

Due to their short stopping times, small dust particles in the solar nebula were not able to settle to the midplane of the disk on short timescales, and thus were initially well mixed with the gas. These small particles, however, did experience Brownian motion, which led to collisions with other particles, and to growth. The larger particles that formed were able to grow massive enough to settle to the nebular midplane on relatively short timescales. These larger objects were also able to continue to grow due to the random motions in the gas as well as the relative velocities they developed with respect to the other particles as they settled at a more rapid rate. It is through these processes that solids began to “rain out” of the nebula, allowing the solid-to-gas ratio at the midplane to increase over time.



Settling of the larger particles would have been retarded if turbulence were present in the disk. Turbulence would have manifested itself as large-scale eddies in the nebular gas which would have lofted particles upward and away from the midplane. The importance of turbulence depends on its strength but, again, small particles would have been most strongly affected, and larger particles would have been able to overcome these motions. The major effect of turbulence is that it increases the minimum particle size needed to make the settling process effective in increasing the solid-to-gas ratio.

In regions of the solar nebula near an evaporation front, midplane temperatures may have been high enough that only vapor was present but, because temperatures decreased with height, solids were present at higher altitudes. As those solids began to coagulate and settle to the midplane, they vaporized once they crossed the evaporation front, reducing the opacity and allowing radiation to escape from the disk more easily, and the gas to cool as a consequence. As a result of this cooling, the evaporation front migrated towards the midplane. The vapor that was present at the edge of the front condensed to form dust that then coagulated, settled and re-vaporized, reducing the opacity even further, repeating the cycle.

Cassen (2001) modeled this coagulation-settling-cooling cycle in the solar nebula and found that the vapor inside the evaporation front became enriched in condensable elements due to the incorporation of solids from above. As the evaporation front descended towards the midplane, the condensables became further concentrated in the vapor as the volume it occupied decreased with time. Immediately before the evaporation front reached the midplane, the vapor reached its peak enhancement in condensables relative to hydrogen, ranging over values of 10 to 120 times the canonical solar ratio, depending on the coagulation rate of the solids. It should be noted that Cassen (2001) reported that enrichment factors in excess of 100 are rare in his models, and that factors of  $\sim 10$  are more likely.

#### Relationship between $f_{O_2}$ of cosmic gases and abundances of C, O and H

In the next two sections, condensation calculations are performed for systems whose abundances of C, O and H became fractionated relative to solar abundances by the mechanisms discussed above. While precise equilibrium values of  $P_{H_2O}/P_{H_2}$  ratios and  $f_{O_2}$ 's are obtained in these computations, the approximations derived in the following discussion allow the reader to understand, at least qualitatively, the relationships between these thermodynamic parameters and the relative abundances of C, O and H. The total pressure of an element  $i$ ,  $P_i^{tot}$ , is defined as the sum of the partial pressures of all species of element  $i$ , multiplied by their respective stoichiometric coefficients. Thus, in the case of hydrogen,

$$P_H + 2P_{H_2} + 3P_{NH_3} + 4P_{CH_4} + \dots = P_H^{tot} \quad (15)$$

In a gas of solar composition, diatomic hydrogen is so much more stable than any other hydrogen-containing molecule that

$$2P_{H_2} \approx P_H^{tot} \quad (16)$$

Furthermore, hydrogen is so much more abundant than any other element that

$$P_{H_2} \approx P^{tot} \quad (17)$$

where  $P^{tot}$  is the total pressure of all species, and

$$P_H^{tot} \approx 2P^{tot} \quad (18)$$

For any element  $i$ ,

$$P_i^{tot} = \frac{A(i)}{A(H)} P_H^{tot} \approx \frac{2A(i)}{A(H)} P^{tot} \quad (19)$$



where  $A(i)$  is the relative atomic abundance of element  $i$  in the Solar System. At high temperature and in the absence of condensates, because  $\text{CO}_{(\text{g})}$  and  $\text{H}_2\text{O}_{(\text{g})}$  are so stable,

$$P_{\text{CO}} \approx P_{\text{C}}^{\text{tot}} \quad (20)$$

and

$$P_{\text{CO}} + P_{\text{H}_2\text{O}} \approx P_{\text{O}}^{\text{tot}} \quad (21)$$

Combining (19), (20) and (21),

$$P_{\text{H}_2\text{O}} \approx \frac{2P_{\text{O}}^{\text{tot}}}{A(\text{H})} [A(\text{O}) - A(\text{C})] \quad (22)$$

If  $K_w$  is the equilibrium constant for the reaction,



then, from (17) and (22),

$$f_{\text{O}_2}^{\frac{1}{2}} = \frac{1}{K_w} \left[ \frac{P_{\text{H}_2\text{O}}}{P_{\text{H}_2}} \right] \approx \frac{2}{K_w} \left[ \frac{A(\text{O}) - A(\text{C})}{A(\text{H})} \right] \quad (24)$$

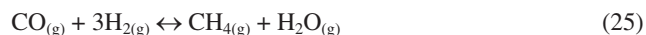
assuming  $f_{\text{O}_2} = P_{\text{O}_2}$ .

The oxygen fugacity of a cosmic gas is thus seen to be dependent not only on the difference between the oxygen and carbon abundances but also on the ratio of this difference to the hydrogen abundance. This is the reason why, in Figure 2, the curves for C/O ratios of 0.42 and 0.43 are so far apart. Although the C/O ratio of Anders and Grevesse (1989) is very similar to the lower limit to that ratio in the Allende Prieto et al. (2001, 2002) studies, both the oxygen and carbon abundances are ~38% lower relative to hydrogen in the latter than in the former.

### Condensation of fayalitic olivine

***FeO in olivine in regions enriched in oxygen by radial transport.*** In the Ciesla and Cuzzi (2006) model, it was assumed that the migrators consisted of equal parts water ice and rock by mass, and that the water ice was the only constituent that vaporized. In this case, the amount of water released from the migrators is 9 times the amount of water already present in the inner solar nebula. As seen in the third column of Table 9, relative to  $1 \times 10^6$  Si atoms, this translates into an increase in the atomic oxygen abundance to  $6.62 \times 10^7$  from  $1.37 \times 10^7$ , and an increase in the atomic hydrogen abundance to  $2.80 \times 10^{10}$  from  $2.79 \times 10^{10}$ . While the atomic abundance of carbon is normal, vaporization of relatively oxygen-rich water ice creates a region of very high oxygen abundance and only slightly higher hydrogen abundance. The reason for the oxygen fugacity enhancement in this case can be seen in the right-hand side of Equation (24).

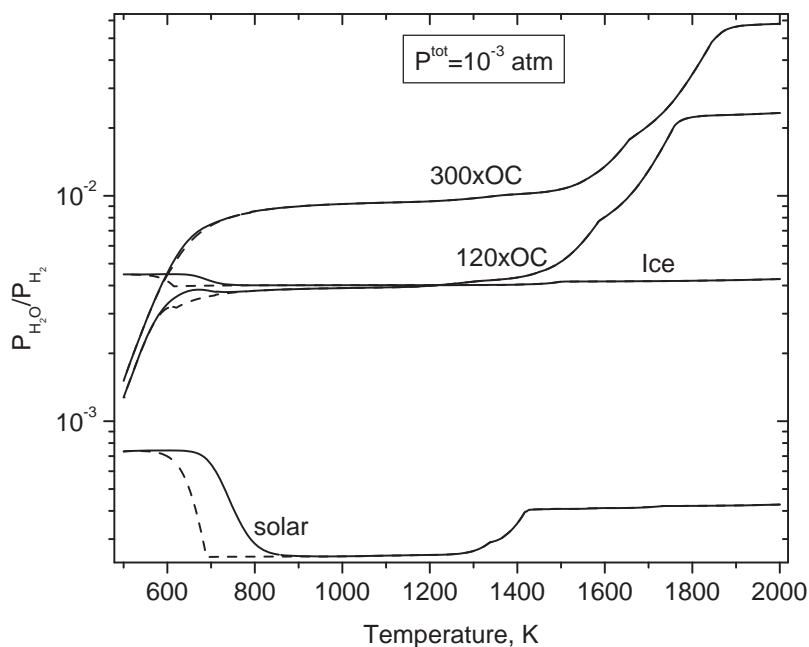
In order to investigate the fayalite content of condensate olivine grains that would be expected in such an ice-enriched environment, a full equilibrium condensation calculation was performed in a system with this composition. The resulting  $P_{\text{H}_2\text{O}}/P_{\text{H}_2}$  ratios are plotted as a function of temperature in Figure 4, together with the ratios in a system of solar composition and in systems enriched in dust by vertical transport processes, all at  $P^{\text{tot}} = 10^{-3}$  atm. Upon equilibrium cooling of all of these systems, a temperature is reached below which a significant fraction of the  $\text{CO}_{(\text{g})}$  begins to form  $\text{CH}_{4(\text{g})}$  via the reaction,



which also increases the  $P_{\text{H}_2\text{O}}/P_{\text{H}_2}$  ratio, making the system more oxidizing. In reality, however, this reaction occurs very slowly, and Prinn and Fegley (1989) argued that the time required for  $\text{CO}_{(\text{g})}$  to be converted to  $\text{CH}_{4(\text{g})}$  would be comparable to the nebular cooling time in this

**Table 9.** Atomic abundances in systems considered in this work.

Element	Solar*	Enriched in ice*	OC*	Enriched in OC by 120×	Enriched in OC by 300×
H	$2.790 \times 10^{10}$	$2.801 \times 10^{10}$	0	$2.790 \times 10^{10}$	$2.790 \times 10^{10}$
He	$2.720 \times 10^9$	$2.720 \times 10^9$	0	$2.720 \times 10^9$	$2.720 \times 10^9$
O	$1.367 \times 10^7$	$6.618 \times 10^7$	$3.750 \times 10^6$	$4.599 \times 10^8$	$1.135 \times 10^9$
C	$6.849 \times 10^6$	$6.849 \times 10^6$	0	$6.849 \times 10^6$	$6.849 \times 10^6$
N	$3.130 \times 10^6$	$3.130 \times 10^6$	0	$3.130 \times 10^6$	$3.130 \times 10^6$
Mg	$1.074 \times 10^6$	$1.074 \times 10^6$	$1.074 \times 10^6$	$1.289 \times 10^8$	$3.222 \times 10^8$
Si	$1.000 \times 10^6$	$1.000 \times 10^6$	$1.000 \times 10^6$	$1.200 \times 10^8$	$3.000 \times 10^8$
Fe	$9.000 \times 10^5$	$9.000 \times 10^5$	$9.000 \times 10^5$	$1.080 \times 10^8$	$2.700 \times 10^8$
S	$4.458 \times 10^5$	$4.458 \times 10^5$	$4.458 \times 10^5$	$5.349 \times 10^7$	$1.337 \times 10^8$
Al	$8.490 \times 10^4$	$8.490 \times 10^4$	$8.490 \times 10^4$	$1.019 \times 10^7$	$2.547 \times 10^7$
Ca	$6.110 \times 10^4$	$6.110 \times 10^4$	$6.110 \times 10^4$	$7.332 \times 10^6$	$1.833 \times 10^7$
Na	$5.740 \times 10^4$	$5.740 \times 10^4$	$5.740 \times 10^4$	$6.888 \times 10^6$	$1.722 \times 10^7$
Ni	$4.930 \times 10^4$	$4.930 \times 10^4$	$4.930 \times 10^4$	$5.916 \times 10^6$	$1.479 \times 10^7$
Cr	$1.350 \times 10^4$	$1.350 \times 10^4$	$1.350 \times 10^4$	$1.620 \times 10^6$	$4.050 \times 10^6$
Ti	$2.400 \times 10^3$	$2.400 \times 10^3$	$2.400 \times 10^3$	$2.880 \times 10^5$	$7.200 \times 10^5$
Co	$2.250 \times 10^3$	$2.250 \times 10^3$	$2.250 \times 10^3$	$2.700 \times 10^5$	$6.750 \times 10^5$

\*Abundances relative to  $10^6$  Si atoms**Figure 4.** Calculated variation of the equilibrium  $P_{\text{H}_2\text{O}}/P_{\text{H}_2}$  ratio (solid curves) with temperature during condensation of a system of solar composition, a system enriched in water ice by a factor of ten relative to solar composition, and systems enriched in dust of OC composition (see Table 9) by factors of 120 and 300 relative to solar composition. Dashed portion of each curve shows the expected departure from the equilibrium trend due to kinetic inhibition of  $\text{CH}_{4(\text{g})}$  formation.

temperature range. In order to correct for this specific case of departure from gas phase equilibrium, each condensation calculation was repeated with  $\text{CH}_{4(g)}$  formation suppressed. For each of the cases considered in Figure 4, the resulting departure of the  $P_{\text{H}_2\text{O}}/P_{\text{H}_2}$  ratio from its respective equilibrium variation is signified by the dashed curve. This effect is seen to be much greater for a system of solar composition than for the ice enrichment case, and is unimportant to the conclusions reached in this work. The  $P_{\text{H}_2\text{O}}/P_{\text{H}_2}$  ratio of the ice-enriched system is seen to be nearly constant with temperature, at  $\sim 4 \times 10^{-3}$ , from 6 to 16 times the ratio for solar composition, depending on temperature.

The difference between the logarithm of the resulting oxygen fugacity and that of the iron-wüstite buffer is plotted in Figure 5 for all of the systems seen in Figure 4 at two different values of  $P^{\text{tot}}$ ,  $10^{-3}$  and  $10^{-5}$  atm. Both the system of solar composition and the ice-enriched one become progressively more oxidizing as the temperature falls, but the ice-enriched one is more oxidizing at all temperatures, by  $\sim 2.4$  log units at 1300 K but only  $\sim 1.5$  log units at 600 K for  $P^{\text{tot}} = 10^{-3}$  atm. In Figure 6 are plotted the fayalite contents of condensate olivine grains that would be in equilibrium with each of these gas compositions as a function of temperature at  $P^{\text{tot}} = 10^{-3}$  atm. In a system of solar composition,  $X_{\text{Fa}}$  of olivine is near zero until the temperature falls below 700 K, and begins to rise steeply with falling temperature only below 550 K. By contrast, the ice-enriched system is sufficiently oxidizing that  $X_{\text{Fa}}$  in its olivine is already  $\sim 0.01$  at 1000 K, begins to rise very steeply below 650 K and reaches 0.15 at  $\sim 610$  K. Because the migrator model ignores the possible presence of C-bearing ices upon whose volatilization the composition of the inner nebula would have become considerably more reducing than

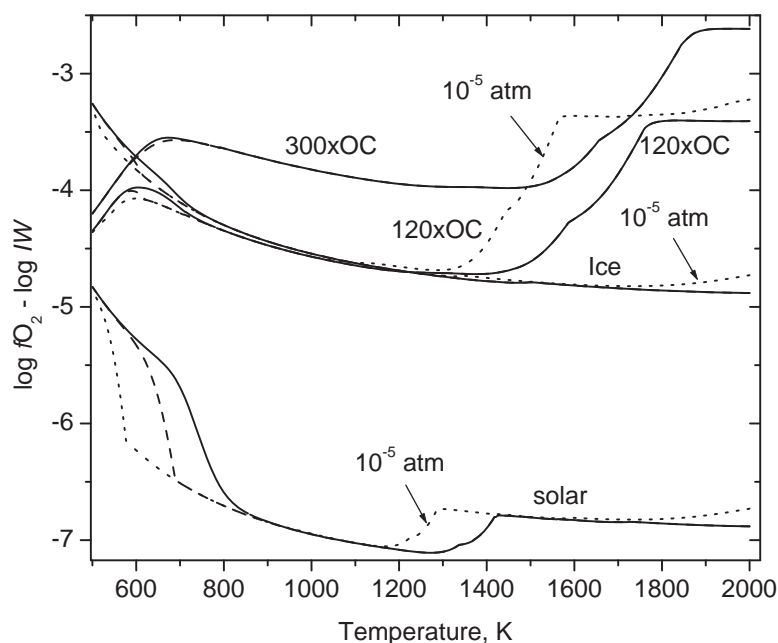


**Figure 5.** Calculated variation with temperature of the logarithm of the equilibrium oxygen fugacity at  $P^{\text{tot}} = 10^{-3}$  atm (solid curves) and at  $P^{\text{tot}} = 10^{-5}$  atm (dotted curves) minus that of the iron-wüstite buffer (Myers and Eugster 1983) during condensation of a system of solar composition, a system enriched in water ice by a factor of ten relative to solar composition, and systems enriched in dust of OC composition by factors of 120 and 300 relative to solar composition. Dashed portions of the curves for  $P^{\text{tot}} = 10^{-3}$  atm show the expected departure from the equilibrium trend due to kinetic inhibition of  $\text{CH}_{4(g)}$  formation.

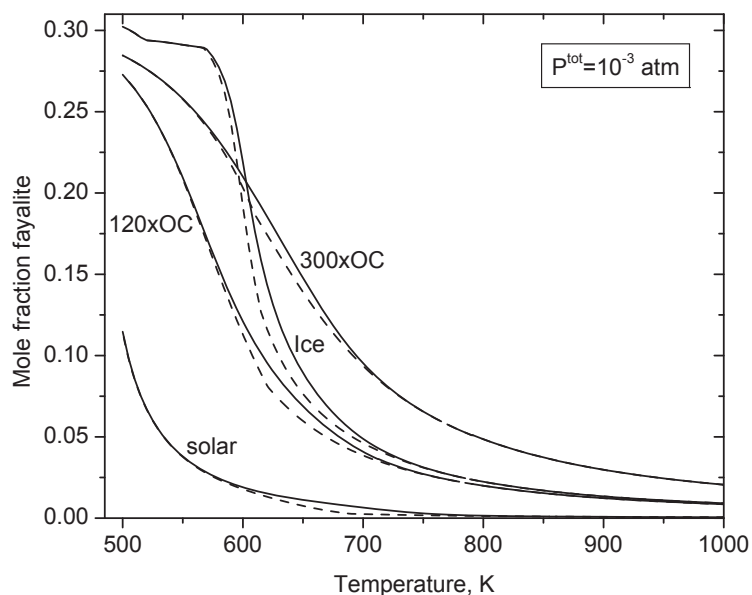


**Figure 6.** Calculated variation with temperature of the equilibrium mole fraction of fayalite in olivine (solid curves) during condensation of a system of solar composition, a system enriched in water ice by a factor of ten relative to solar composition, and systems enriched in dust of OC composition by factors of 120 and 300 relative to solar composition. Dashed portion of each curve shows the expected departure from the equilibrium trend due to kinetic inhibition of  $\text{CH}_4(\text{g})$  formation.

indicated by the curves in Figure 5, the  $X_{\text{Fa}}$  values shown for the ice-enriched case in Figure 6 should be regarded as upper limits.

Fedkin and Grossman (2006) showed that, because Fe-Mg interdiffusion coefficients in olivine are very small, especially when extrapolated to temperatures where the equilibrium  $X_{\text{Fa}}$  becomes significant, olivine condensate grains of finite size would not have been able to reach the homogeneous fayalite contents predicted by equilibrium calculations. For a slow cooling and a fast cooling model, in which the cloud cools exponentially with time from 1500 K at decay constants of  $4.32 \times 10^{-6}$  and  $4.32 \times 10^{-5} \text{ yr}^{-1}$ , respectively, they showed that only the edges of the grains would have reached the equilibrium  $X_{\text{Fa}}$ , but that  $X_{\text{Fa}}$  in their interiors would fall progressively further behind the equilibrium value with falling temperature, resulting in chemically zoned crystals. Using the same cooling rate models, the same computational technique and the same dependence of the interdiffusion coefficient on  $X_{\text{Fa}}$ , temperature and  $f_{\text{O}_2}$  as were used by Fedkin and Grossman (2006), the development of fayalite zoning profiles was calculated for grains whose radii are 0.1  $\mu\text{m}$  in the ice-enriched system. Results are shown in Figure 7, where they are compared with those calculated for grains of the same size in a system of solar composition. In the ice-enriched system, the concentration profile for the slow cooling case becomes invariant at 715 K, where the equilibrium  $X_{\text{Fa}}$  is 0.041 and the mean  $X_{\text{Fa}}$  of the grains, obtained from the area under the profile, is 0.019. For fast cooling, the profile is frozen in at 750 K, where the equilibrium  $X_{\text{Fa}}$  is 0.031 and the mean  $X_{\text{Fa}}$  of the grains is 0.015. Thus, although the mean  $X_{\text{Fa}}$  values predicted for very tiny olivine grains that cooled at very slow rates in the ice-enriched parts of the nebula envisioned by Ciesla and Cuzzi (2006) are a factor of 20 greater than those seen for grains of the same size that cooled at the same rate in a system of solar composition, and are similar to those of many olivine grains in Type I chondrules, they are still an order of magnitude smaller than the mean  $X_{\text{Fa}}$  of the precursors of chondrules in ordinary chondrites, 0.15.

In order to investigate the maximum possible effect of evaporation from radial migrators on the  $f_{O_2}$  of the inner solar nebula, its bulk composition was calculated assuming evaporation of not only the ice but also the rocky part of the migrators. The rocky part was assumed to contain solar proportions of all elements with condensation temperatures equal to or greater than that of S. All S was assumed to be present as FeS, and all excess Fe was converted to FeO. When such material, whose composition is shown in column 4 of Table 9 and is referred to as OC in the present work, condenses in a system of solar composition, it contains 27% of the oxygen and none of the carbon or hydrogen. It was found that the remaining 73% of the

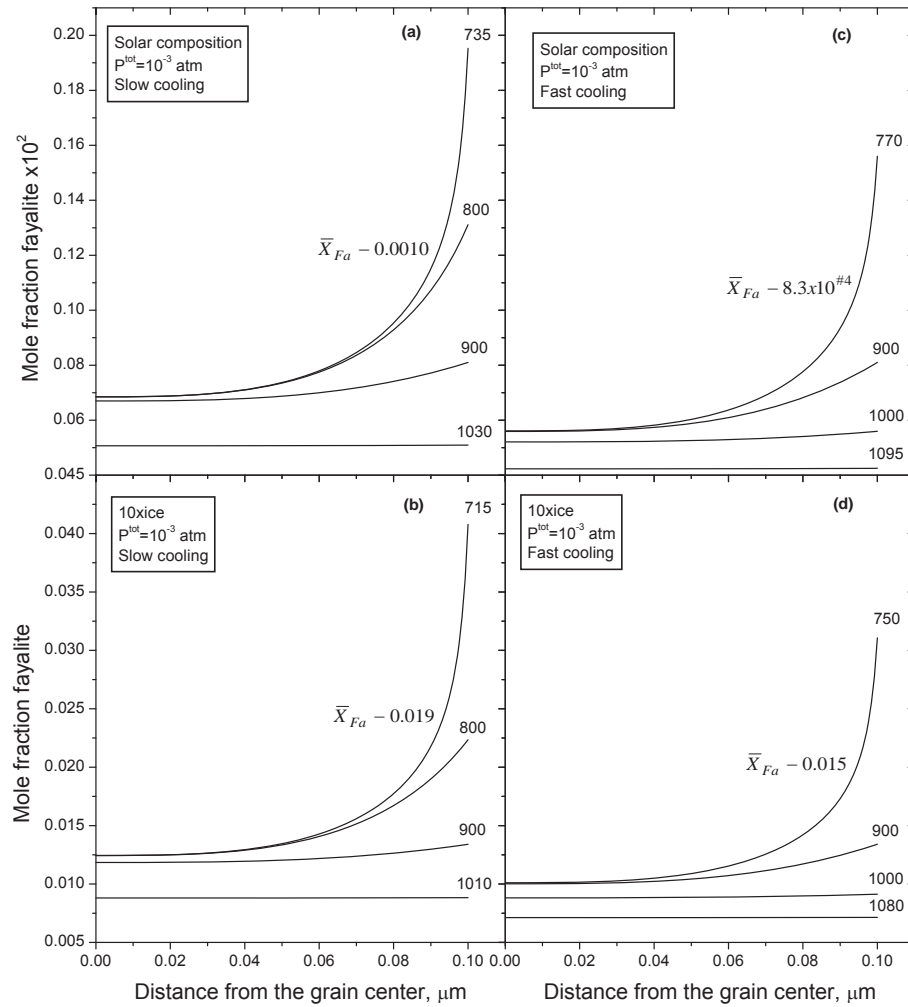


**Figure 7.** Calculated variation of fayalite concentration with distance from the centers of olivine grains with radii of  $0.1 \mu\text{m}$  whose surfaces are in equilibrium with the gas in a system of (a, c) solar composition and in a system (b, d) enriched by a factor of ten in water relative to hydrogen due to radial transport of icy migrators. Profiles are shown at several temperatures during exponential cooling with decay constants of (a, b)  $4.32 \times 10^{-6} \text{ yr}^{-1}$  and (c, d)  $4.32 \times 10^{-5} \text{ yr}^{-1}$  along the  $f_{O_2}$ - $T$  path for each system composition. In each case, the temperature at which each profile was calculated is given in K, and the curve labeled with the mean  $X_{Fa}$  of the grain is the profile for the temperature below which diffusion becomes negligible.

oxygen is not quite sufficient to make migrators having equal parts of water ice and OC rock by mass, but that, when all remaining oxygen was consumed, the migrators were composed of 48.6% ice. The composition of a region resulting from total evaporation of migrators of this composition was calculated in such a way that the water abundance was enriched by a factor of ten from the ice component alone. Because there is so much more oxygen in the ice component than in the rocky part of the migrators, the oxygen abundance of the system only increases by 30% when the rocky part of the migrators is evaporated in addition to the ice. When the gas speciates, the  $P_{\text{H}_2\text{O}}/P_{\text{H}_2}$  ratio and the resulting  $\log f_{\text{O}_2}$  are very little different from the curves shown in Figures 4 and 5 for the case of ice evaporation alone.

***FeO in olivine in regions enriched in oxygen by vertical transport.*** Strictly speaking, the coagulation and settling model of Cassen (2001) applies to nebular regions where the midplane temperature was greater than the forsterite condensation temperature. Although the temperature was lower at higher altitudes, it is unlikely that it became low enough for water to condense until much time had passed and the settling process was nearly over. In this case, the dust composition was assumed to be that of OC. In the Cassen (2001) model, such dust was enriched relative to the gas by a maximum factor of 120 compared to solar abundances in a midplane region, and was totally vaporized. Condensation calculations were performed in systems enriched by a factor of 120 and a factor of 300 in OC dust. The compositions of these systems are shown in columns 5 and 6 of Table 9. Because of the relatively large amount of oxygen in the dust and the assumed absence of carbon and hydrogen from it, significant enhancements in  $f_{\text{O}_2}$  are again expected in systems of these compositions based on Equation (24). This is the so-called “dust enrichment” effect first pointed out by Wood (1967).

For each of these systems, the variation of the  $P_{\text{H}_2\text{O}}/P_{\text{H}_2}$  ratio as a function of temperature during condensation is shown in Figure 4. Upon cooling in a system of solar composition, the equilibrium  $P_{\text{H}_2\text{O}}/P_{\text{H}_2}$  ratio begins to decline just above 1400 K due to the onset of forsterite condensation, which removes a significant fraction of the oxygen from the vapor. This phenomenon has very little effect in the ice-enriched system because of its much greater bulk O/Si ratio (Table 9) than solar composition, but it occurs at a higher temperature and produces a much larger decline in the  $P_{\text{H}_2\text{O}}/P_{\text{H}_2}$  ratios in the OC dust-enriched systems because they have much smaller O/Si ratios than solar composition. Below 800 K, the equilibrium  $P_{\text{H}_2\text{O}}/P_{\text{H}_2}$  ratio increases sharply in solar composition due to a shift to the right in the CO-H<sub>2</sub>O equilibrium, Equation (25). This effect is muted in the ice-enriched system because the O/C ratio is so much larger than in solar composition. Below 800 K in the dust-enriched systems, the  $P_{\text{H}_2\text{O}}/P_{\text{H}_2}$  ratios begin to decline sharply due to oxidation of metallic iron. For the case of enrichment in OC dust by a factor of 120, the enhancement of the  $P_{\text{H}_2\text{O}}/P_{\text{H}_2}$  ratio is about a factor of 15 relative to the solar case in the 700-1200 K temperature interval, very similar to that of the ice-enriched system, but falls sharply below 600 K. For enrichment by a factor of 300, the enhancement in the  $P_{\text{H}_2\text{O}}/P_{\text{H}_2}$  ratio is ~30.

The difference between the logarithm of the resulting oxygen fugacity and that of the iron-wüstite buffer is plotted in Figure 5 for each of these systems. While the  $10^{-3}$  atm and  $10^{-5}$  atm curves for the ice-enriched system are nearly coincident, depression of the olivine condensation temperature at  $10^{-5}$  atm causes the relatively high  $P_{\text{H}_2\text{O}}/P_{\text{H}_2}$  ratio, and therefore  $\log f_{\text{O}_2}$ , at high temperature to persist to lower temperatures than at  $10^{-3}$  atm in both the solar case and in the system enriched in OC dust by a factor of 120. Because Equation (25) shifts to the right at lower temperature at  $10^{-5}$  atm than at  $10^{-3}$  atm, the increase in the  $P_{\text{H}_2\text{O}}/P_{\text{H}_2}$  ratio, and therefore  $\log f_{\text{O}_2}$ , begins at a lower temperature at  $10^{-5}$  atm. At  $P^{\text{tot}} = 10^{-3}$  atm, the oxygen fugacities of systems enriched by factors of 120 and 300 in OC dust are ~2.4 and ~3.1 log units more oxidizing, respectively, than that of a system of solar composition at the same temperature within the 700-1500 K temperature interval but this difference narrows sharply below 700 K.

The equilibrium  $X_{\text{Fa}}$  of olivine in these systems is shown in Figure 6. In the case of enrich-

ment in OC dust by a factor of 120,  $X_{Fa}$  is very similar to that in the ice-enriched system above 700 K but rises less steeply below this temperature, reaching 0.15 at 585 K. When the dust/gas enrichment factor is increased to 300, 2.5 times the largest enrichment found by Cassen (2001), the equilibrium  $X_{Fa}$  reaches 0.05 at 800 K and 0.15 at 640 K. Fayalite concentration profiles for 0.1  $\mu\text{m}$ -radius grains were calculated as above for each of the systems enriched in OC dust for each cooling model. Results are shown in Figure 8. For the case of enrichment by a factor of 120 under slow cooling conditions, the concentration profile becomes invariant at 720 K, where

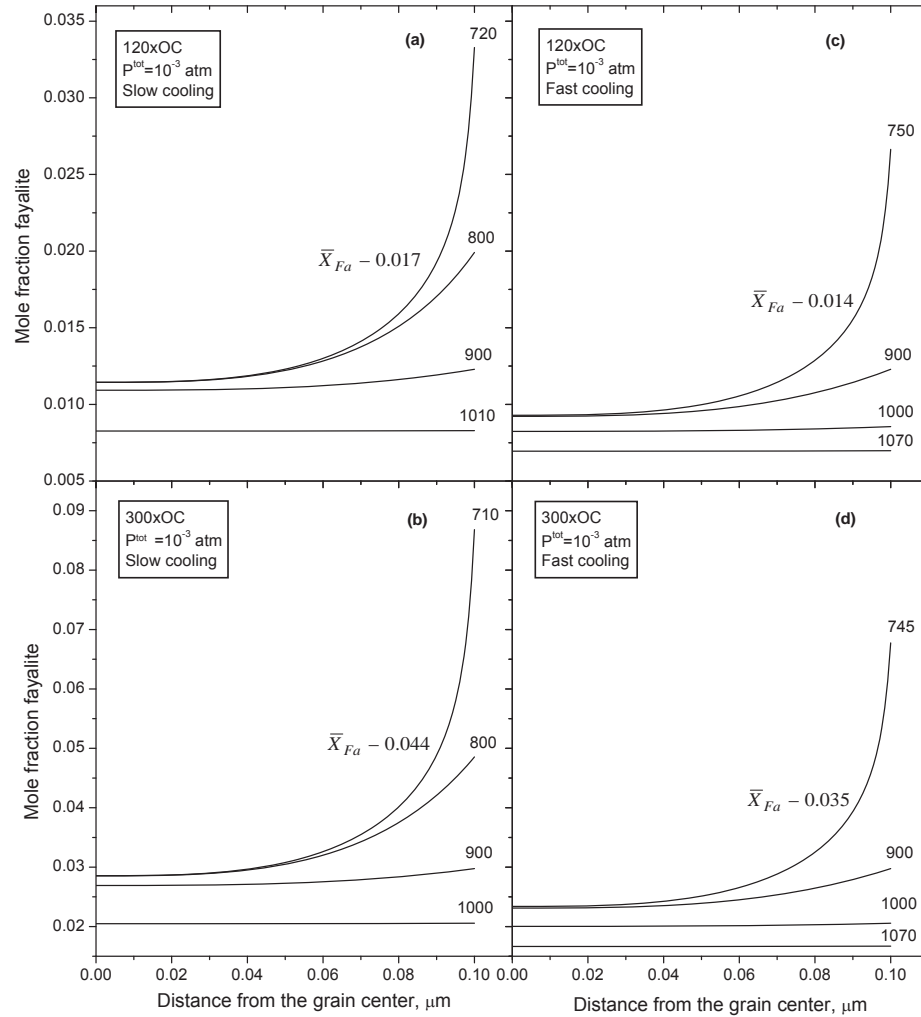


**Figure 8.** Calculated variation of fayalite concentration with distance from the centers of olivine grains with radii of 0.1  $\mu\text{m}$  whose surfaces are in equilibrium with the gas in a system enriched in OC dust by a factor of (a, c) 120 and (b, d) 300 compared to solar composition due to coagulation and vertical settling. Profiles are shown at several temperatures during exponential cooling with decay constants of (a, b)  $4.32 \times 10^{-6} \text{ yr}^{-1}$  and (c, d)  $4.32 \times 10^{-5} \text{ yr}^{-1}$  along the  $f_{O_2}$ -T path for each system composition. In each case, the temperature at which each profile was calculated is given in K, and the curve labeled with the mean  $X_{Fa}$  of the grain is the profile for the temperature below which diffusion becomes negligible.



the equilibrium  $X_{\text{Fa}}$  is 0.033 and the mean  $X_{\text{Fa}}$  of the grains is 0.017. For fast cooling, the profile is frozen in at 750 K, where the equilibrium  $X_{\text{Fa}}$  is 0.027 and the mean  $X_{\text{Fa}}$  of the grains is 0.014. When very tiny grains undergo cooling at very low rates in a system enriched in dust relative to gas by the maximum amount found by Cassen (2001) in his coagulation and settling model, the predicted  $X_{\text{Fa}}$  of the olivine is far short of the mean  $X_{\text{Fa}}$  of the precursors of chondrules in ordinary chondrites. Even if dust/gas enrichments of 300 relative to solar composition are considered, the predicted  $X_{\text{Fa}}$  still falls short. The concentration profiles for this case are also shown in Figure 8, from which it is seen that the predicted mean  $X_{\text{Fa}}$  is only 0.044 for slow cooling and 0.035 for fast cooling, a factor of  $\sim 4$  too low. Extrapolation of the slow cooling data for 0.1  $\mu\text{m}$  grains suggests that the coagulation and settling model could account for the required  $X_{\text{Fa}}$  only if it could achieve enrichments in dust relative to gas of a factor of  $\sim 1000$  relative to solar composition. The results presented for a system of this composition by Fedkin and Grossman (2006) yielded mean  $X_{\text{Fa}}$  of only 0.093, but this was for grains of radius 1.0  $\mu\text{m}$ .

**The need for greater fractionation of oxygen.** The oxygen enrichment models investigated above do not yield nebular regions that are sufficiently oxidizing to stabilize FeO at temperatures high enough for Fe-Mg interdiffusion in olivine to be rapid compared to the nebular cooling time. In one way of overcoming this problem, Fedkin and Grossman (2006) postulated primitive dust having the composition of 10 parts C1 chondrite and 1 part water ice. In a nebular region enriched in such material by a factor of 125 relative to solar composition, resulting in a  $\log f_{\text{O}_2}$  of IW-2.4 at a reference temperature of 1500 K, olivine grains with radii of 3  $\mu\text{m}$  would have reached an  $X_{\text{Fa}}$  of 0.14 before diffusion stopped, even for fast cooling. The oxygen abundance enhancement assumed in that case, however, is much higher than is possible in the icy migrators model reviewed here. No dynamic process is known that can enrich a nebular region in ice by such a large factor. The best way to make FeO-bearing olivine crystals many microns in size, like those seen in primitive meteorites, on time-scales much shorter than the cooling time of the solar nebula is in a process that not only occurs at coincidentally high  $f_{\text{O}_2}$  and high temperature but also causes condensation of the olivine under those conditions, thus eliminating the diffusion problem altogether. One such process was illustrated by Ebel and Grossman (2000), who showed that silicate liquid + olivine with  $X_{\text{Fa}} \geq 0.15$  are stable condensates at  $T > 1400$  K and  $10^{-6} < P^{\text{tot}} < 10^{-3}$  bar in systems enriched in dust of C1 chondrite composition by a factor  $> 500$ . It should be noted that this dust is more oxygen-rich than the OC composition considered above and that the dust/gas enrichment factor is much greater than has been created in any dynamical model. The corresponding  $\log f_{\text{O}_2} \geq \text{IW}-1.8$ , considerably greater than those produced at 1400 K in any of the dynamical models considered above, as can be seen in Figure 5.

**Other means of creating oxidizing environments.** Starting with a homogeneous nebula of solar composition, no way has been found of fractionating oxygen from carbon and hydrogen by an amount that could create a region of sufficiently high  $f_{\text{O}_2}$  to account for the FeO/(FeO + MgO) ratio of the precursors of chondrules in UOCs. Other possibilities are considered in the next three sections.

- *Inherited chemical heterogeneity.* Perhaps the solar nebula inherited spatial heterogeneities in the relative abundances of carbon, oxygen and hydrogen from its parent interstellar cloud. If so, the key parameter is in the right-hand side of Equation (24),  $[A(\text{O})-A(\text{C})]/A(\text{H})$ , which has a value of  $4.9 \times 10^{-4}$  for solar composition. In order to achieve the minimum  $f_{\text{O}_2}$  found by Fedkin and Grossman (2006) to be necessary for diffusion of an adequate amount of  $\text{Fe}^{2+}$  into pre-existing forsterite under the conditions described in the previous section, this parameter has to be  $\sim 0.036$ . Similarly, to reach the minimum  $f_{\text{O}_2}$  found by Ebel and Grossman (2000) to be necessary for direct condensation of olivine with  $X_{\text{Fa}} = 0.15$  under the conditions described in the previous paragraph, it has to be at least  $\sim 0.12$ . The required values of  $[A(\text{O})-A(\text{C})]/A(\text{H})$  represent enhancements by factors of  $\sim 70$  and  $\sim 240$ , respectively, relative to solar composition. Whether chemical heterogeneities of this size could

be present in the parent interstellar cloud, whether they could survive its collapse, and whether they could persist in the solar nebula until condensation occurred are unknown. The effect of initial heterogeneity on fractionations produced in radial and vertical transport models should be investigated.

- *Vaporization of dust in a reconnection ring.* Neither coagulation, vertical settling and evaporation of condensate dust nor evaporation of water ice from horizontally transported migrators can enrich nebular regions sufficiently in oxygen relative to hydrogen and carbon to account for the relatively high FeO content of the precursors of chondrules in ordinary chondrites. Recall, however, that, in the X-wind model of Shu et al. (2001), the protosolar magnetosphere, a region of relatively low gas density, is the site of evaporation of relatively large amounts of dust, producing a vapor in the reconnection region whose dust/gas enrichment factor is  $\sim 25000$ , according to S. Desch (pers comm). In the same condensation calculations used above to show that such an environment is far too oxidizing to stabilize  $\text{Ti}^{3+}$ -bearing fassaite in refractory inclusions, olivine begins to condense at 1410 K. Its  $X_{\text{Fa}}$  is  $\sim 4 \times 10^{-4}$  initially, but reaches 0.047 at 1200 K and 0.29 at 1000 K. It thus appears that the X-wind model is capable of generating sufficiently oxidizing conditions at moderate temperatures to stabilize olivine having the fayalite content required of chondrule precursors. In this case, however, all of the Mg and Si are condensed as forsterite and enstatite by  $\sim 1200$  K, so the increase in the  $X_{\text{Fa}}$  of the olivine to values  $> 0.047$  predicted at equilibrium below 1200 K must occur by Fe-Mg interdiffusion in the olivine. Although the condensation time-scale in the reconnection region is only  $\sim 1$  day, the diffusion coefficients are much higher in this temperature interval than at the lower temperatures considered above. As a result, the mean  $X_{\text{Fa}}$  of  $0.1 \mu\text{m}$  radius grains reaches  $\sim 0.09$  before diffusion stops, reasonably close to the mean  $X_{\text{Fa}}$  of chondrule precursors. Alternatively, if rapid cooling in such a region caused olivine condensation to be delayed by  $\sim 235$  K due to supercooling, grains with the required mean  $X_{\text{Fa}}$  could have condensed directly out of the gas, and diffusion of additional  $\text{Fe}^{2+}$  would be unnecessary. Caution should be exercised in concluding that this is the solution to the problem, however, as this prediction is based on application of equilibrium thermodynamics to condensation in an environment subjected to repeated ionization by solar flares, where the equilibrium assumption would not be expected to hold.
- *Photolysis of  $\text{CO}_{(\text{g})}$ .* Clayton (2005) suggested another idea, also based on interaction of the protosun with matter in the innermost part of the nebular disk. He argued that mass-independent variations of oxygen isotopic compositions observed in refractory inclusions and chondrules may be the result of isotopic self-shielding during photodissociation of  $\text{CO}_{(\text{g})}$  by UV radiation from the young Sun. According to this model, at some distance from the Sun, a nebular region would exist where destruction of  $\text{CO}_{(\text{g})}$  would produce monatomic oxygen greatly and approximately equally enriched in  $^{17}\text{O}$  and  $^{18}\text{O}$  relative to  $^{16}\text{O}$ , and that this could be the source of the oxygen which exchanged with nebular condensates and chondrules to produce isotopic compositions at the high- $^{18}\text{O}$  end of the CCAM line. Clayton (2005) suggested that the observed correlation between  $\text{FeO}/(\text{FeO} + \text{MgO})$  ratio and enrichment in  $^{17}\text{O}$  and  $^{18}\text{O}$  within individual chondrites and among the different chondrite chemical classes is a consequence of a process that affected both parameters. In this view, photolysis of  $\text{CO}_{(\text{g})}$  molecules is not only responsible for the mass-independent oxygen isotopic variations but also for creating a much more oxidizing environment than a normal solar gas with equilibrium speciation, not by increasing the  $P_{\text{H}_2\text{O}}/P_{\text{H}_2}$  ratio significantly but by increasing the partial pressure of monatomic oxygen by a large factor. Lyons (2006) calculated the photolytically induced variation of the relative abundances of gas species in the system H-O-He as a function of height above the nebular midplane

that would be expected at a heliocentric distance of 3 AU at 800 K and  $1.6 \times 10^{-6}$  bar for an enhancement of the protosolar UV flux by a factor of  $10^3$  relative to the modern Sun. While virtually all of the oxygen is present as  $\text{H}_2\text{O}$  at the midplane, its photolysis products increase in abundance with height, until virtually all of the oxygen is monatomic above a height of 0.6 AU.

Evaluating these ideas is difficult. Ebel and Grossman (2001) investigated the relative thermodynamic stabilities of condensates in a system of solar composition in which no polyatomic gas molecules were allowed to form. Entirely different condensates form at high temperature, including more  $\text{SiO}_2$ -rich and more FeO-rich minerals, than those seen in equilibrium calculations. Although this is a poor analogy to the situation envisioned by Clayton (2005) in that thermodynamic equilibrium between gas and minerals was assumed in the absence of equilibrium gas-phase speciation and no ionized species were considered, it does demonstrate that completely different mineral assemblages could prevail in systems far from equilibrium, including those that contain high FeO at high temperature.

#### Change of FeO/(FeO + MgO) during chondrule melting

**Reduction of FeO-bearing, non-equilibrium condensates.** For the case of enrichment in oxygen by evaporation of water ice from radial migrators, what would the continued evolution of the system be like beyond the point where the magnesium silicates fail to equilibrate with the gas because of slow diffusion? One could imagine a nebular region containing a fine-grained mixture of forsterite, enstatite, feldspars  $[(\text{Ca},\text{Na})\text{Al}(\text{Al},\text{Si})_3\text{O}_8]$ , feldspathoids and metallic nickel-iron. As the temperature continues to fall, troilite ( $\text{FeS}$ ) condenses, coating some of the metal grain surfaces, and the magnesium silicates become more unstable. Eventually, the water will condense as water ice and/or by hydrating magnesium silicates, and may oxidize exposed metal grain surfaces, forming considerable amounts of FeO. If clumps of such relatively oxidized material were then heated, further mineralogical evolution of this material would depend on the temperature to which it was heated, the time spent at high temperature and the composition of the surrounding gas. If it were melted in vacuum for an hour or less, for example, fayalitic olivine would be one of the resulting phases, as seen in some of the Wang et al. (2001) evaporation experiments. If, instead, it were melted in the gas from which it condensed, it might eventually reach an equilibrium state characterized by the relatively low  $f_{\text{O}_2}$  and  $X_{\text{Fa}}$  corresponding to the temperature at which it was heated on the curves labeled “ice” in Figures 5 and 6, respectively. If, however, the time spent above the solidus were short compared to the reduction time, olivine with a higher  $X_{\text{Fa}}$  than the equilibrium value would be a likely product.

Everything else being equal, the higher the  $f_{\text{O}_2}$  of the ambient gas, the slower the rate of reduction would be, and the longer the heating time that would allow persistence of relatively fayalitic olivine. Unmelted, or relict, olivine grains discovered in some chondrules in primitive chondrites by Nagahara (1981) and Rambaldi (1981) have higher  $X_{\text{Fa}}$  than olivine that apparently crystallized from their host chondrule melts. Rambaldi suggested that the tiny metallic Fe inclusions found inside these so-called “dusty” olivine grains are a product of partial reduction of the FeO in the relict olivine, showing that the FeO/(FeO + MgO) ratios of the precursors of at least some chondrules in primitive chondrites were modified during chondrule formation, in this case to lower values. Jones and Danielson (1997) measured the amount of metallic Fe in the dusty regions of relict olivine grains. For a final  $X_{\text{Fa}}$  of 0.01 to 0.06, they estimated that the precursors of those grains had values of  $X_{\text{Fa}}$  ranging from 0.06 to 0.11 based on 2 vol % metal, the minimum metal content they found, and from 0.26 to 0.29 based on 9%, the maximum. Leroux et al. (2003) synthesized dusty olivine by heating olivine with  $X_{\text{Fa}} = 0.16$  at 1610 °C and  $\log f_{\text{O}_2} = -15.2$ , 0.5 log units below that of a system of solar composition at the same temperature. Due to reduction of FeO, which formed  $\mu\text{m}$ -sized blebs of metallic Fe,  $X_{\text{Fa}}$  of the associated olivine fell to 0.058 in five minutes and 0.001 in 100 minutes, time-scales comparable to chondrule cooling times.

What fraction of the precursor material of each chondrule and of the chondrule population as a whole underwent this process is unknown. Johnson (1986) assumed, as did Wood (1967), that most iron in chondrule precursors was oxidized, that chondrule formation occurred by melting in a relatively reducing nebular gas, that individual chondrules cooled before their FeO could be totally reduced, and that the very wide range of  $X_{\text{Fa}}$  exhibited by the chondrules in individual UOCs and carbonaceous chondrites is a record of the range in the degree of reduction experienced by those objects. Johnson (1986) performed precise electron microprobe analyses of coexisting olivine and low-Ca pyroxene in the chondrules of five different chondrites, assumed that the lowest-FeO grains she found had reached equilibrium with the surrounding gas, and calculated its  $f_{\text{O}_2}$  from Equation (13). At 1500 K, the lowest and highest  $\log f_{\text{O}_2}$ 's are  $-17.3$  in Chainpur and  $-15.4$  in Krymka, respectively, corresponding to 0.9 and 2.8 log units above that of a solar gas at the same temperature. Relaxation of the assumption that the FeO/(FeO + MgO) ratio remains invariant during chondrule formation shifts the question away from how to make systems rich enough in oxygen to produce fayalitic olivine precursors. The question now becomes how to make the gas compositions with which chondrule melts approached equilibration. Plotting Johnson's (1986) results on Figure 5 shows that the required  $f_{\text{O}_2}$  for the Chainpur chondrules is readily achievable in both the water ice-enriched system and the system enriched in OC dust by a factor of 120 at  $10^{-3}$  and  $10^{-5}$  atm, but the Krymka data can be accounted for only in the latter system at  $10^{-5}$  atm. The facts that silicate liquid is unstable in all three systems, metal is unstable in the dust-enriched system at  $10^{-5}$  atm and that olivine of any composition is unstable in the ice-enriched system at 1500 K serve to underscore the importance of the kinetics of mineral transformations and silicate evaporation to theories of this kind. Nevertheless, the theory of Wood (1967) and Johnson (1986) seems not only capable of accounting for the wide range of  $X_{\text{Fa}}$  in chondrules but also requires systems enriched in oxygen by amounts that are within the range of those produced in nebular transport models. Whether the rate of redox equilibration of chondrule melts with their ambient gas relative to the rates of metal and silicate evaporation during typical chondrule thermal histories is permissive of this kind of theory remains to be determined (Fedkin et al. 2006).

In a TEM study of the matrix of ALHA77307, the least equilibrated CO3 chondrite, Brearley (1993) found regions of siliceous amorphous material containing abundant, 0.1 to 0.3  $\mu\text{m}$  olivine grains whose  $X_{\text{Fa}}$  varies from 0.09 to 0.69, along with similarly-sized grains of kamacite, pyrrhotite and magnetite. If nebular formation of fayalitic olivine can only be accomplished by incomplete reduction of FeO in chondrule melts, all of this matrix olivine would have to have been derived from chondrules as well, a phenomenon that is hard to imagine. Although indigenous hydrated silicates are absent from Brearley's assemblage, it may be related to the non-equilibrium, low-temperature condensates postulated above, and might be a good candidate for an oxidized precursor for chondrules. Brearley (1993) suggested that the olivine grains in this material formed by incipient annealing of the amorphous phase prior to accretion. This again points to the need for a very oxidizing nebular gas.

**Oxidation of reduced chondrule precursors.** Jones (1990) argued that the partially resorbed forsterite cores of some olivine crystals in Type II chondrules in Semarkona are relict grains. If true, this indicates, in contrast to the above examples, that at least one precursor component of these chondrules may have formed at *lower*  $f_{\text{O}_2}$  than that which prevailed during crystallization of the bulk of the material in their host chondrules. This leads to the alternative hypothesis that, in these chondrules, the olivine crystals with the highest, rather than the lowest, fayalite contents are the ones that approached high-temperature equilibrium with the surrounding gas most closely. As discussed above, this would require enrichments in oxygen-rich (C1) dust relative to gas by factors  $>500$  compared to solar abundances, much greater than can be produced in radial and vertical transport models. In the context of a shock-wave model for chondrule melting, Cuzzi and Alexander (2006) calculated that chondrule-sized particles would have had to be enriched by factors of 300-500 in order to suppress isotopic fractionation

of relatively volatile elements. It is interesting that the magnitudes of these enrichments approach those needed for nebular equilibration of assemblages consisting of silicate liquid + olivine with  $X_{\text{Fa}} \geq 0.15$ , but these workers found that only a small proportion of chondrules can be so concentrated by their favored mechanism, turbulent concentration.

Zanda et al. (1994) found that the concentrations of Si and Cr in metal correlate directly with one another and inversely with the FeO content of olivine in the chondrules of primitive chondrites, and suggested, as did Scott and Taylor (1983), that the distributions of these elements between metal and silicate were established during chondrule formation. Using the dependences of these distributions on  $f_{\text{O}_2}$ , Zanda et al. (1994) found that values of  $\log f_{\text{O}_2}$  derived from each of the three elemental distributions were in reasonable agreement with one another, and varied from  $-8.4$  to  $-12.2$  from one chondrule to another at a reference temperature of 1873 K. This range of values is from 6.3 to 2.5 log units more oxidizing than a system of solar composition at the same temperature. Similarly, a value of  $-12.5$  was calculated at the same temperature from the Si content of a metal grain in Bishunpur, which was inferred by Lauretta et al. (2001) to have come from a Type I chondrule. Based on experimental simulations of chondrule melting and crystallization, Connolly et al. (1994) suggested that the reducing agent responsible for both dusty olivines and the observations of Zanda et al. (1994) was reduced carbon that was present in the chondrule precursor material. If so, the  $f_{\text{O}_2}$ 's estimated from these studies may represent internal  $f_{\text{O}_2}$ 's generated during chondrule formation, and may thus have little or no relation to the  $f_{\text{O}_2}$  of the surrounding gas, such as might be expected if the time-scale for chondrule formation were too rapid for significant gas-droplet interaction. The degree to which reducing agents in chondrule precursors affected the compositions of chondrule minerals and estimates of  $f_{\text{O}_2}$ 's derived from them depends on the amounts of reducing agents initially present, and these are unknown.

Lauretta et al. (2001) sought to determine the gas composition responsible for formation of fayalite + troilite assemblages on the edges of kamacite grains in the Bishunpur chondrite, using thermodynamic calculations and kinetic constraints. At the derived temperature of  $\sim 1200$  K,  $P^{\text{tot}}$  of  $\sim 10^{-5}$  bar and elemental composition of the gas, the equilibrium  $P_{\text{H}_2\text{O}}/P_{\text{H}_2}$  ratio is  $\sim 0.27$ . This value, very far off the scale of Figure 4, is well beyond the values achievable in any of the nebular transport models considered here.

## REDOX CONDITIONS INFERRED FROM OTHER IRON-BEARING NEBULAR MATERIALS

### Amoebooid olivine aggregates

Amoebooid olivine aggregates are fine-grained mixtures of Ca- and Al-rich phases, such as spinel and aluminous diopside, with olivine and metallic nickel-iron. These objects have been interpreted as aggregates of nebular condensates (e.g. Grossman and Steele 1976; Krot et al. 2004a,b) but, since  $\text{Ti}^{3+}$  has not been detected in their clinopyroxene, it is not certain that they condensed in a system of solar composition. According to Krot et al. (2004b), most olivine in AOAs in the least metamorphosed CO3 chondrites, ALHA77307, Acfer 094 and Adelaide, has  $X_{\text{Fa}} \leq 0.02$  but values up to 0.15 are known from ALHA77307. The lowest  $X_{\text{Fa}}$  reported in AOAs in Acfer 094 is  $\sim 0.002$  (Krot et al. 2004a). An  $X_{\text{Fa}}$  as low as 0.002 is only twice as large as the maximum that can be expected for olivine that formed in a system of solar composition (Fig. 7a), but this value is based upon  $10^6$ -yr cooling times and grain radii of only 0.1  $\mu\text{m}$ . Petrographic study of AOAs in these objects reveals patches of olivine up to 5  $\mu\text{m}$  in diameter (Chizmadia et al. 2002). Unless these patches underwent post-condensation grain coarsening or FeO metasomatism, an origin by condensation in a system of solar composition can only be entertained if they are composed of crystallites  $\ll 0.1$   $\mu\text{m}$  in radius.



### Metal grains in CH chondrites

Using a combined condensation, grain growth and diffusion model, Petaev et al. (2003) and Petaev (2006) calculated fits to concentration profiles of major, minor and trace elements in zoned grains of metallic nickel-iron in CH chondrites. In the latest calculations (Petaev 2006), the best fits to the profiles in a metal grain in PAT91456 were obtained under the assumption that it is a direct condensate from a system enriched in dust relative to gas by only a factor of 3 compared to solar composition. From the dust composition used by Petaev et al. (2003), a plausible case can be made from this calculation that the grain condensed from a system whose  $f_{\text{O}_2}$  was one full log unit greater than that of a system of solar composition. This conclusion is non-unique, however, as it depends on a number of assumptions, on physico-chemical data such as diffusion coefficients and activity coefficients which are uncertain, as well as on a number of adjustable parameters such as  $P^{\text{tot}}$ , degree of isolation of various condensate phases, cooling rate and size of grain nucleus which are unknown. If, on the other hand, the grain could be shown to be part of an equilibrium assemblage containing an element in two valence states whose activity ratio had been experimentally calibrated as a function of  $f_{\text{O}_2}$ , the  $f_{\text{O}_2}$  would be known with such certainty that its value could be used to constrain the adjustable parameters.

## FORMATION CONDITIONS OF ENSTATITE CHONDRITES

### Mineralogy of EH3 enstatite chondrites

The EH3s are the least equilibrated enstatite chondrites. According to Nehru et al. (1984), Parsa, a typical member of this group, contains ~57 wt% enstatite, 17% metallic nickel-iron, 14% troilite, 6% plagioclase, 4% forsterite, 1.4% silica ( $\text{SiO}_2$ ), 0.6% schreibersite ( $\text{Fe}_3\text{P}$ ), 0.6% daubreeite ( $\text{FeCr}_2\text{S}_4$ ), 0.4% oldhamite ( $\text{CaS}$ ) and 0.1% niningerite ( $\text{MgS}$ ). Using mineral composition and modal abundance data for several EH3 chondrites, Wasson, Kallemeyn and Rubin (unpublished data) calculated that 64% of the Ca is in oldhamite, and 4% of the Mg in niningerite. Lusby et al. (1987) showed that approximately half the pyroxene grains in these meteorites contain  $\leq 1$  mol% ferrosilite ( $\text{FeSiO}_3$ ), the FeO-rich end-member of the low-Ca pyroxene solid solution series. Of the clear pyroxene grains, those free of tiny metal blebs that indicate post-crystallization reduction, 92-96% contain  $< 5$  mol%  $\text{FeSiO}_3$ . The presence of sulfides of normally lithophile elements like Mg, Ca and Cr; very small amounts of FeO in most of the enstatite; and up to 3.6 wt% Si in the metal phase all suggest that these objects formed at very low  $f_{\text{O}_2}$ .

### Condensation at high C/O ratio

Unlike the ordinary chondrites, which seem to require a higher  $f_{\text{O}_2}$  than is possible in a system of solar composition, condensation of unequilibrated enstatite chondrites requires a lower  $f_{\text{O}_2}$  than can be generated from solar composition. Larimer (1975) and Larimer and Bartholomay (1979) were the first to show that phases such as oldhamite, graphite (C) and SiC would replace oxides and silicates as high-temperature condensates in systems whose compositions are solar except for elevated atomic C/O ratios of 0.91 or more. The reason for this phenomenon lies in the extreme stability of  $\text{CO}_{(\text{g})}$ , which causes this molecule to consume virtually the entirety of whichever of C and O is the lower in abundance, leaving the excess of the more abundant element to form other molecules and condensates. For solar composition,  $\text{C/O} = 0.5$ , leading to Equation (20). Equation (21) shows that virtually all of the excess oxygen is present as  $\text{H}_2\text{O}_{(\text{g})}$ . Equation (22) shows that  $P_{\text{H}_2\text{O}}$ , and thus the oxygen available for condensates, is approximately proportional to the difference between the oxygen and carbon abundances. As a result of this, if the abundance of carbon approaches that of oxygen in a system otherwise solar in composition, the amount of available oxygen shrinks, causing the condensation temperatures of oxides and silicates to fall and those of graphite, carbides, nitrides and sulfides to increase until the latter

become the highest-temperature condensates when the C/O ratio  $\sim 0.95$ . This is illustrated in Figure 9, which shows some of the results of equilibrium condensation calculations performed over a narrow range of atomic C/O ratios for such a system using the program employed by Fedkin and Grossman (2006), which contains more modern thermodynamic data than were available to Larimer (1975) and Larimer and Bartholomay (1979). Those workers ascribed the unusual mineralogy of enstatite chondrites to formation in a system whose C/O ratio is slightly elevated above the solar value. The question is by how much.

As seen from Equation (24), the  $f_{O_2}$  is also expected to become vanishingly small as the abundance of carbon approaches that of oxygen. This is illustrated in Figure 10, where the variation with temperature of the equilibrium  $\log f_{O_2}$  taken from the above condensation calculations is plotted for a variety of C/O ratios. The unusually large breaks in the slopes of some of these curves are all caused by condensation reactions that either draw down or release gaseous oxygen, phenomena that would not normally have such a marked effect on  $f_{O_2}$  at lower C/O ratios where there is more available oxygen. On the curve for C/O = 0.85, for example, the break in slope at  $\sim 1290$  K is caused by the onset of forsterite condensation. At C/O = 0.96, the sudden increase in  $\log f_{O_2}$  at  $\sim 1390$  K is due to release of oxygen from  $SiO_{(g)}$  with the onset of condensation of Si-bearing metallic nickel-iron. That increase is broken at 1380 K when  $TiC_{(c)}$  begins to react with gaseous nitrogen and oxygen to form  $TiN_{(c)}$  and  $CO_{(g)}$ . At C/O = 0.98, the rate of decrease of  $\log f_{O_2}$  is broken due to release of oxygen from the breakdown of  $CO_{(g)}$  accompanying condensation of SiC at  $\sim 1550$  K and graphite at  $\sim 1060$  K. At temperatures above condensation temperatures, it can be seen that the rate of decrease of  $\log f_{O_2}$  with increasing C/O

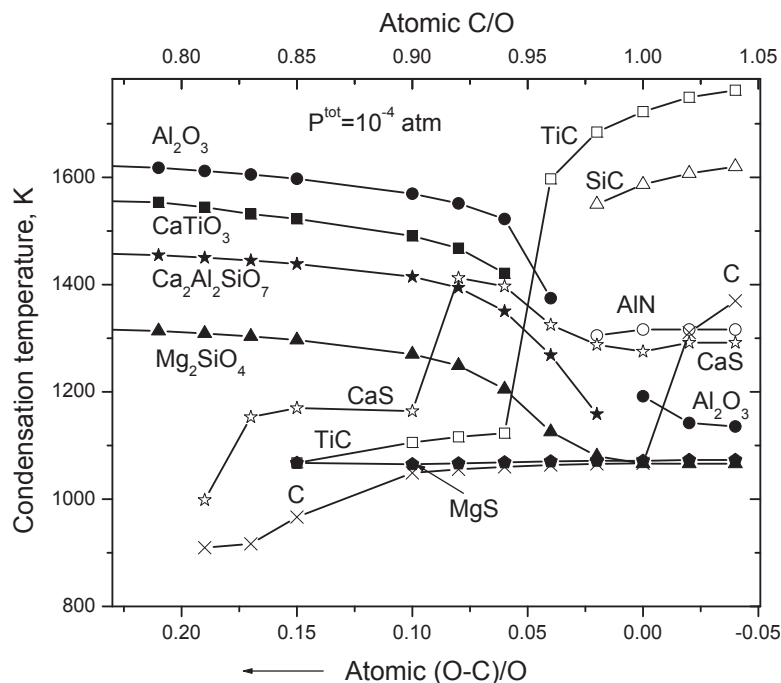


**Figure 9.** Equilibrium condensation temperatures at  $P^{tot} = 10^{-4}$  atm as a function of the fraction of the total oxygen abundance in excess of the carbon abundance. As the carbon abundance approaches the oxygen abundance in a system otherwise solar in composition, condensation temperatures of oxides and silicates decrease, and those of sulfides, carbides and nitrides increase. The corresponding C/O ratios are shown along the top of the diagram. The solar C/O ratio is 0.5.



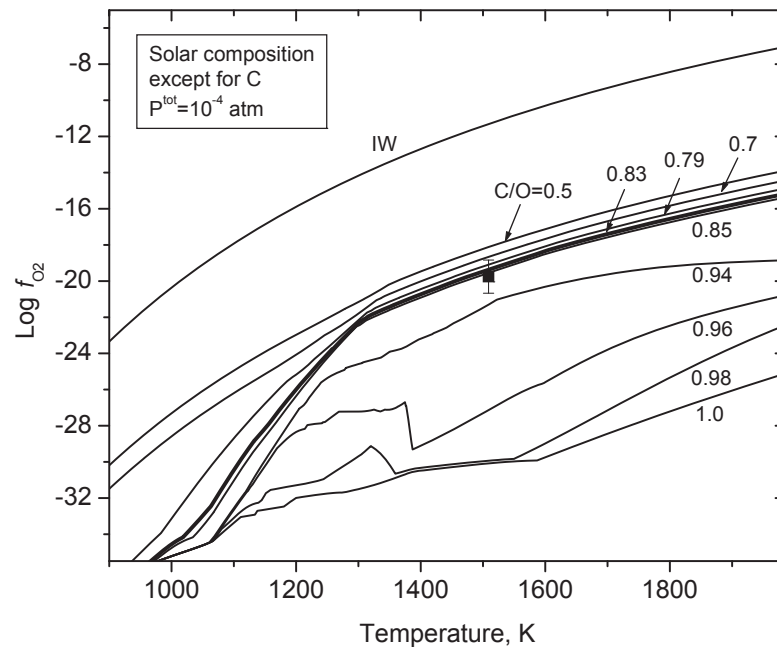


**Figure 10.** Equilibrium  $\log f_{\text{O}_2}$  plotted against temperature at  $P^{\text{tot}} = 10^{-4}$  atm for systems of solar composition except for the carbon abundance. For temperatures above those where condensation reactions produce discontinuities on the curves,  $\log f_{\text{O}_2}$  at a given temperature falls slowly with increasing C/O ratio at first, then much more rapidly. Unlike the other curves, the bold curve at an atomic C/O ratio of 0.83, which is most compatible with the mineralogy of EH3 chondrites, includes the effect of removal of high-temperature condensates at 1258 K. The iron-wüstite buffer curve, IW, is shown for reference, as is the data point obtained from fassaite in CAIs.

ratio increases as the C/O ratio increases. At 1600 K, for example, increasing the C/O ratio by 40% relative to the solar value, to 0.70, causes a decrease in  $f_{\text{O}_2}$  of less than one log unit but an increase of only 2%, from 0.94 to 0.96, causes a decrease in  $f_{\text{O}_2}$  of more than 5 log units.

Two observations indicate that enstatite chondrites condensed from a system whose C/O ratio was not greatly different from the solar value. First, the maximum Si content of metal grains in EH3 chondrites is only a factor of 30 higher than that found in metal in the Murchison CM2 chondrite, 0.12 wt%, by Grossman et al. (1979). Those workers showed further that condensation from a system with atomic C/O = 0.55 can account for metal with Si contents up to ~0.17 wt%. Everything else being equal, the maximum Si content of condensate metal varies inversely as  $f_{\text{O}_2}^{1/2}$ . This suggests that the  $f_{\text{O}_2}$  needed to account for the Si content of metal grains in enstatite chondrites is ~2 or 3 log units lower than that of a system of solar composition. From Figure 10, such  $f_{\text{O}_2}$ 's correspond to C/O ratios between 0.90 and 0.94, slightly below those where dramatic changes in the mineralogy of high-temperature condensates occur (Fig. 9). Also, at high C/O ratios, the condensation calculations summarized in Figure 9 yield large proportions of high-temperature phases which are not found in EH3 chondrites, such as graphite, SiC and sinoite ( $\text{Si}_2\text{N}_2\text{O}$ ). In particular, if the C/O ratio were  $\geq 1.02$ , graphite would condense above 1310 K and, before disappearing at ~750 K, would consume more than 22% of the carbon, making it more abundant by mass than enstatite. This would also be the case if the C/O ratio were increased by decreasing the abundance of oxygen rather than by increasing that of carbon. Because of the relatively large amount of graphite that is predicted

to form, its wide stability field and the relatively low temperature at which it would disappear at equilibrium, at least some residue of graphite might be expected to persist in EH3 chondrites had they formed under these conditions.

### Bulk chemical compositions of EH enstatite chondrites

At equilibrium, forsterite ( $\text{Mg/Si} = 2$ ) and enstatite ( $\text{Mg/Si} = 1$ ) are the dominant, high-temperature, Mg- and Si-containing condensates in systems close to solar in composition. Forsterite condenses at a higher temperature and, because the atomic Mg/Si ratio of the system is close to 1 (1.07 in solar composition), forsterite begins to react with the relatively Si-enriched gas at a lower temperature to form enstatite. The resulting ratio of enstatite to forsterite is dictated by the Mg/Si ratio of the system and the amounts of Mg and Si consumed in coexisting phases. When enstatite begins to form in a system of solar composition, the fraction of the total Si that is used to make coexisting anorthite + Ca-rich clinopyroxene is about four times that of the Mg, resulting in a molar forsterite/enstatite ratio of  $\sim 0.30$  (Yoneda and Grossman 1995). This translates to a forsterite/enstatite weight ratio of  $\sim 0.42$ . This is much greater than the weight ratio of 0.07 observed in EH3 chondrites. The very low modal proportions of forsterite relative to enstatite are reflected in the bulk chemical compositions of enstatite chondrites, whose atomic Mg/Si ratios are  $\sim 26\%$  less than that in C1 chondrites (Larimer and Anders 1970). Also, their atomic Al/Si, Ca/Si and Ti/Si ratios are each  $\sim 46\%$  less (Larimer and Anders 1970) and their Fe/Si ratios  $\sim 8\%$  greater than those of C1 chondrites (Wasson 1985). Larimer and Anders (1970) attributed these element depletions to removal of early, higher-temperature condensates in the form of refractory Ca-, Al-, Ti-rich phases, metallic nickel-iron and forsterite from the region where enstatite chondrites were condensing. Removal of forsterite, in particular, would produce a depletion in the Mg/Si ratio relative to C1 chondrites and therefore in the forsterite/enstatite ratio of the residual condensate. In fact, Petaev and Wood (1998) predicted just such an effect on the residual condensate for some conditions of continuous removal of early condensates from reactive contact with the gas, and suggested that enstatite chondrites formed by this process in a system of solar composition.

### Condensation of EH enstatite chondrites

To investigate possible formation of enstatite chondrites by condensation from a cooling gas with slightly enhanced C/O ratio, a condensation calculation was performed at  $P^{\text{tot}} = 10^{-4}$  atm and an atomic C/O ratio of 0.83. The distribution of Ca, Mg and Si between crystalline phases and vapor are shown as functions of temperature in Figures 11, 12 and 13, respectively. Under these conditions, an alloy of Fe, Ni and Si begins to condense at 1370 K. All Al, Ca and Ti are condensed as Ca-aluminates, perovskite and melilite by 1350 K, as is readily seen in Figure 11. When the temperature has fallen to 1258 K, the latter phases have all reacted to form spinel + Ca-rich pyroxene, 50% of the Mg has condensed in forsterite (see Fig. 12) and 95% of the Fe in metallic nickel-iron. Single-stage removal from equilibrium of 67% of the spinel + Ca-rich pyroxene, 100% of the forsterite and 37% of the metal phase at that temperature results in a residual system whose Ca/Si, Al/Si and Ti/Si ratios are 0.55, Mg/Si ratio is 0.74 and Fe/Si ratio is 1.08 relative to C1 chondrites, very close to the values of these ratios in EH3 chondrites. Subsequent condensation was modeled as a closed system, equilibrium process. After removal of high-temperature condensates, gaseous silicon is depleted by condensation of forsterite and simultaneous dissolution in the pre-existing metallic nickel-iron, as can be seen in Figure 13. At equilibrium, Ca-rich pyroxene is predicted to begin to react with  $\text{H}_2\text{S}_{(\text{g})}$  to form oldhamite, spinel and forsterite at 1155 K, and, when the temperature has fallen to 1132 K, all Ca is present as oldhamite. At 1060 K, residual  $\text{Mg}_{(\text{g})}$  condenses as niningerite. This phase accounts for a maximum of 11% of the magnesium before it begins to react to form forsterite, and disappears completely at 955 K. The silicon content of the metal phase reaches its maximum value at 1018 K, where it begins to be consumed together with silicon from  $\text{SiS}_{(\text{g})}$  and forsterite to form sinoite. The latter phase ultimately consumes 50% of the total silicon

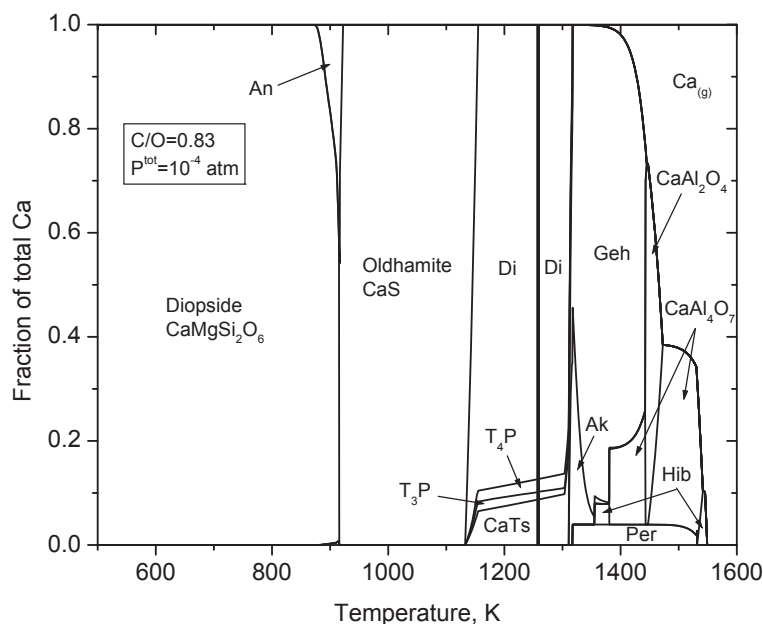


**Figure 11.** Distribution of Ca between crystalline phases and vapor as a function of temperature at  $P^{\text{tot}} = 10^{-4}$  atm in a system whose composition is solar except for an atomic C/O ratio of 0.83. The bold vertical line is the vapor-solid equilibration temperature of the phases removed in a single stage, below which phase proportions are computed as a fraction of the residual Ca. Abbreviations: Hib-hibonite,  $\text{CaAl}_{12}\text{O}_{19}$ ; Per-perovskite,  $\text{CaTiO}_3$ ; Geh-gehlenite,  $\text{Ca}_2\text{Al}_2\text{SiO}_7$ ; Ak-åkermanite,  $\text{Ca}_2\text{MgSi}_2\text{O}_7$ ; Di-diopside; CaTs-Ca-Tschermak's pyroxene,  $\text{CaAl}_2\text{SiO}_6$ ;  $\text{T}_4\text{P-Ti}^{4+}$ -bearing pyroxene,  $\text{CaTiAl}_2\text{O}_6$ ;  $\text{T}_3\text{P-Ti}^{3+}$ -bearing pyroxene,  $\text{CaTiAlSiO}_6$ ; An-anorthite,  $\text{CaAl}_2\text{Si}_2\text{O}_8$ .

in the residual system before disappearing in a series of reactions. At 922 K, sinoite begins to react with  $\text{Na}_{(\text{g})}$  and CaS to form plagioclase, and at 916 K, Ca-rich pyroxene begins to form from sinoite, the anorthite component of plagioclase and oldhamite. At 911 K, forsterite and sinoite begin to react to form enstatite, exhausting the sinoite almost immediately and the forsterite by 893 K. Small amounts of pure silica and forsterite become stable over different temperature intervals below 900 K, and troilite forms at 721 K.

The variation of the Si content of the metal phase is plotted as a function of temperature in Figure 14, where it is compared to that for several other C/O ratios at  $P^{\text{tot}} = 10^{-4}$  atm. The present calculations employ the activity coefficients of Si measured by Sakao and Elliott (1975) between 1373 and 1643 K in  $\alpha$ -Fe alloys containing between 1.4 and 4.2 wt% Si and no Ni. While the equilibration temperatures and Si contents of the predicted alloys overlap these ranges, extrapolation of the activity coefficient data to temperatures as low as 900 K and Si contents as high 10 wt% may involve large uncertainties. Also, Vogel and Palme (2004) found a significant dependence of the activity coefficient of Si on Ni content for Fe-Ni-Si alloys containing <1 wt% Si at  $T \geq 1573$  K. For all except the very highest temperature alloys predicted here, the Ni contents are between 4 and 6 wt%, but were assumed to have no effect on the Si activity coefficient. When the Sakao and Elliott (1975) data are extrapolated to the high temperatures and low Si contents of the Vogel and Palme (2004) study, the former data are in excellent agreement with the latter for alloys with zero Ni content at 1673 K, a factor of 2 higher at 1623 K, and a factor of 4 higher at 1573 K. At each C/O ratio in Figure 14, high-temperature condensates were removed in a single stage in amounts appropriate to generate

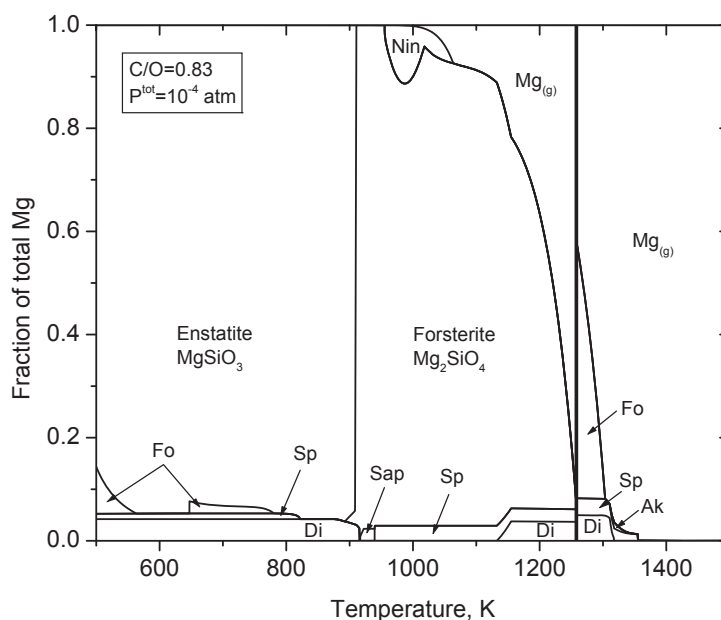


**Figure 12.** Distribution of Mg between crystalline phases and vapor as a function of temperature at  $P^{\text{tot}} = 10^{-4}$  atm in a system whose composition is solar except for an atomic C/O ratio of 0.83. The bold vertical line is the vapor-solid equilibration temperature of the phases removed in a single stage, below which phase proportions are computed as a fraction of the residual Mg. Abbreviations: Sp-spinel,  $\text{MgAl}_2\text{O}_4$ ; Fo-forsterite; Nin-ninningerite,  $\text{MgS}$ ; Sap-sapphirine,  $\text{Mg}_4\text{Al}_{10}\text{Si}_2\text{O}_{23}$ . Others as used previously.

the Ca/Si, Al/Si, Ti/Si, Mg/Si and Fe/Si ratios observed in enstatite chondrites, as in the above example. For the case considered above,  $\text{C/O} = 0.83$ , the Si content of the first-condensing metal is 0.4 wt%, rises with falling temperature to a maximum of 10 wt% and then falls to zero as sinoite, enstatite and silica consume the available silicon. In this case, the equilibrium Si content of the metal exceeds 3.6 wt%, the maximum reported for EH3 chondrites, over a temperature interval of 300 K. Similar curves are shown for other C/O ratios, with the maximum Si content increasing with increasing C/O ratio.

In summary, if specific amounts of high-temperature condensates are removed from further interaction with the vapor in a system whose  $P^{\text{tot}} = 10^{-4}$  atm and whose composition is solar except for a C/O ratio of 0.83, condensates from the residual system can be produced whose bulk major element composition is that of enstatite chondrites. Furthermore, those condensates have very large ratios of enstatite to forsterite and several wt% Si in the coexisting metallic nickel-iron phase, two characteristic features of the predominant mineral constituents of EH3 chondrites. Also seen in EH3 chondrites are small amounts of free silica and albite ( $\text{NaAlSi}_3\text{O}_8$ )-rich feldspar, and the predicted condensates would contain small amounts of these phases also, if reactions continued to temperatures as low as 800-900 K. A very similar condensate assemblage was calculated by Hutson and Ruzicka (2000), who modelled condensation of E3 chondrites in a system from which refractory silicate condensates and 85% of the  $\text{H}_2\text{O}_{(\text{g})}$  were removed at high temperature. In that work, the fractionation of  $\text{H}_2\text{O}_{(\text{g})}$  led to an atomic C/O ratio of  $\sim 0.78$ , close to that adopted here by C addition.

There are, however, features of the predicted condensate assemblages that are inconsistent with the mineralogical compositions of these meteorites. Sinoite is predicted to have a stability

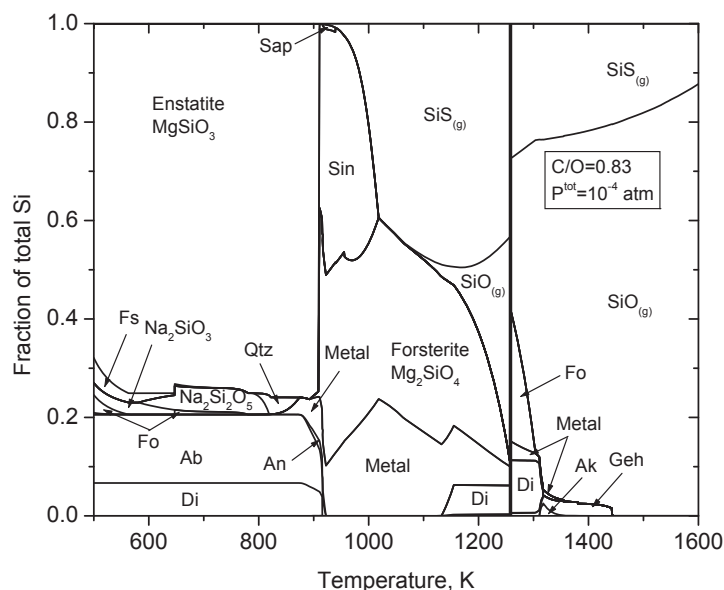


**Figure 13.** Distribution of Si between crystalline phases and vapor as a function of temperature at  $P^{\text{tot}} = 10^{-4}$  atm in a system whose composition is solar except for an atomic C/O ratio of 0.83. The bold vertical line is the vapor-solid equilibration temperature of the phases removed in a single stage, below which phase proportions are computed as a fraction of the residual Si. Abbreviations: Sin-sinoite,  $\text{Si}_2\text{N}_2\text{O}$ ; Ab-albite,  $\text{NaAlSi}_3\text{O}_8$ ; Qtz-quartz,  $\text{SiO}_2$ ; Fs-ferrosilite- $\text{FeSiO}_3$ . Others as used previously.

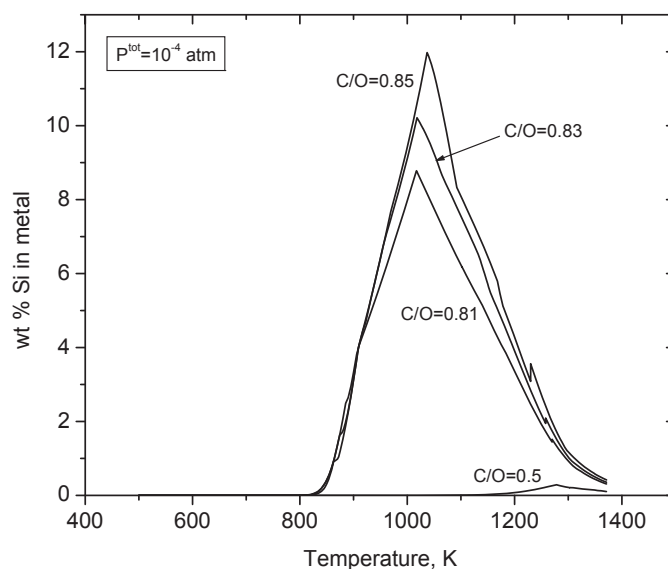


**Figure 14.** Calculated equilibrium concentration of Si in metallic nickel-iron as a function of temperature at  $P^{\text{tot}} = 10^{-4}$  atm in systems of various C/O ratios but whose compositions are otherwise solar. In each case, the discontinuity between 1200 and 1300 K marks the temperature at which appropriate amounts of early condensates were removed to yield condensates with bulk compositions like those of EH chondrites. The curve obtained in the case of closed-system, equilibrium condensation in a system of solar composition, atomic C/O = 0.5, is shown for reference.

field more than 100 K wide, and to consume up to 50% of the total silicon before reacting to form enstatite at 911 K; yet, none is found in EH3 chondrites. Oldhamite is predicted to consume 100% of the Ca before reacting away to form plagioclase and Ca-rich pyroxene at 916 K; yet, only ~64% of the Ca is in oldhamite in EH3 chondrites. Similarly, while as much as 11% of the Mg is predicted to form niningerite before it disappears in a reaction to form forsterite and spinel at 955 K, only ~4% of the Mg in EH3 chondrites is present as this phase. It could be argued perhaps that much less than the equilibrium amounts of these phases formed because of reaction rate difficulties at the relatively low temperatures where oldhamite is predicted to begin forming by reaction from Ca-rich pyroxene, 1155 K, and where niningerite begins condensing, 1064 K. Or it may be that, once they formed, less than the total amount of the oldhamite and niningerite reacted away at the even lower temperatures where they would have disappeared at equilibrium. It could also be argued that all of the sinoite reacted with forsterite to form enstatite at 911 K, but the low temperature at which this is predicted to occur makes this explanation unlikely. This poses an important problem for this model, not only in explaining the complete absence of sinoite from EH3 chondrites but also in explaining how their major constituent, enstatite, was able to consume almost all of the original forsterite. If, on the other hand, EH3 chondrites condensed at a lower C/O ratio; e.g., at 0.81, the temperature at which sinoite and forsterite disappear would increase by only 50 K but the stability fields of both CaS and MgS would disappear completely. At higher C/O ratios, the stability fields of the sulfides expand but the temperature of enstatite formation falls even lower than at C/O = 0.83. This is a specific example of the general kinetic problem of condensing oxides and silicates at high C/O ratios, a problem caused by the characteristic depression of their condensation temperatures relative to those in a system of solar composition, particularly at C/O  $\geq$  0.90 (Fig. 9). It is possible that the thermodynamic data for some of these relatively exotic phases are uncertain by sufficient amounts that stability fields for CaS and MgS may exist at a C/O ratio where enstatite formation occurs at a higher temperature.

#### Formation conditions of EH3 enstatite chondrites

If the constituents of EH3 chondrites condensed in a system with a C/O ratio of 0.83, log  $f_{O_2}$  was IW-8.9 before removal of high-temperature condensates, but varied from ~IW-10.1 at 1200 K to ~IW-13 at 900 K after grain removal increased the C/O ratio of the residual gas (Fig. 10). Formation of such a system requires enrichment of a nebular region in carbon relative to oxygen by 66% compared to solar composition. It is interesting to note that each of the mechanisms described above for enriching nebular regions in oxygen relative to carbon also creates complementary regions depleted in oxygen relative to carbon. While it is tempting to associate the condensation site of EH3 chondrites with these complementary regions, the latter cannot be responsible. The mechanism for oxygen depletion is condensation of oxygen into silicates at relatively low temperatures in the coagulation and settling models, and into water ice at even lower temperatures in the radial migrators case, followed by transport of the oxygen-containing condensates to other regions in both cases. The compositions of the oxygen-depleted regions would have been even more strongly depleted in all other condensable elements than they would have been in oxygen, and thus could not have supported condensation of EH3 chondrites.

The most frequently encountered ferrosilite content in pyroxene from EH3 chondrites is ~1 mol%, with values ranging as high as an amazing 34% (Weisberg et al. 1994). Ferrosilite contents in excess of trace levels are completely incompatible with the formation conditions derived here based on the Si content of the metal and the presence of CaS and MgS, raising the possibility that different constituents of these meteorites formed under different redox conditions, possibly in different nebular regions. Lusby et al. (1987) and Weisberg et al. (1994) presented petrographic evidence for partial reduction of the FeO-rich pyroxene into metallic iron and pyroxene with lower FeO content, implying that the relatively FeO-rich pyroxene formed

under oxidizing conditions but, at a later stage, was exposed to more reducing conditions. Ebel and Alexander (2005) performed condensation calculations in a system enriched in “C-IDP” dust, an analog to anhydrous cluster IDPs, identical to the OC composition used in this work but with sufficient carbon added to yield an atomic C/Si ratio of 0.7561. In a system enriched by a factor of 1000 in C-IDP dust, the C/O ratio is quite low,  $\sim 0.20$ , and partial pressures of condensables are quite high, causing FeO-rich olivine and pyroxene to condense with silicate liquid at high temperature. As the temperature falls, however, a large fraction of the oxygen condenses in silicates while carbon remains in the gas, and the  $f_{\text{O}_2}$  falls sharply, leading to reduction of previously condensed FeO and condensation of oldhamite and niningerite above 1000 K. At high temperature, the curve of  $\log f_{\text{O}_2}$  vs. temperature lies well above the curve for C/O = 0.83 shown in Figure 10 but approaches the latter with falling temperature and is nearly coincident with it between 1400 and 1150 K. Thus, Ebel and Alexander (2005) found a novel way of accounting for the two-stage redox history recorded by pyroxene in EH3 chondrites without appealing to mixing of materials formed in distinct nebular regions with different  $f_{\text{O}_2}$ ’s but the magnitude of the dust enrichment required to do so is much higher than has been produced in vertical transport models, and it is not known whether removal of FeO-bearing, high-temperature condensates could yield a residue with the combination of bulk Mg/Si and Fe/Si ratios observed in EH3 chondrites.

## CONCLUSIONS

Crystallization experiments on liquids with compositions similar to those of compact Type A, Type B1 and Type B2 refractory inclusions were conducted under controlled temperature and  $f_{\text{O}_2}$  conditions. Application of the results to the compositions of coexisting  $\text{Ti}^{3+}$ -bearing fassaite clinopyroxene + melilite pairs in natural examples of these inclusion types shows that, if they crystallized at  $\sim 1509$  K, they did so at  $\log f_{\text{O}_2} = -19.8 \pm 0.9$ . This is only slightly below the equilibrium  $\log f_{\text{O}_2}$  calculated for a partially condensed system of solar composition at the same temperature,  $-18.1^{+0.2}_{-0.3}$ , or IW-6.8. Fassaite is the only  $f_{\text{O}_2}$  indicator that shows that anything in chondrites formed in a system that was close to solar in composition. Solar composition is so reducing that metallic nickel-iron is the stable condensed form of iron over a very wide temperature range. Equilibrium calculations predict vanishingly small amounts of condensed FeO until temperatures fall below 800 K, where the FeO/(FeO + MgO) ratio of the condensate begins to increase very gradually with falling temperature by oxidation of metallic iron and formation of fayalite in solid solution in previously condensed forsterite. The mechanism for the latter process is diffusion of  $\text{Fe}^{2+}$  through the crystal structure of forsterite, but the diffusion rate is nearly zero at these temperatures. By comparison to what is achievable in a system of solar composition, the mean FeO/(FeO + MgO) ratio of the olivine in chondrules in unequilibrated ordinary chondrites is very high,  $\sim 0.15$ . Making such ratios in chondrule precursors by solar nebular processes requires sufficiently high  $f_{\text{O}_2}$  for iron to become oxidized above temperatures where diffusion of  $\text{Fe}^{2+}$  becomes very low. In an attempt to do so, dynamic models have been proposed for enrichment of oxygen relative to carbon and hydrogen in specific nebular regions. Two such models were investigated quantitatively in the present work: radial transport of water ice-rich migrators across the snow line into the inner part of the solar nebula where the ice evaporates; and coagulation, vertical settling and evaporation of anhydrous dust in the median plane of the inner nebula. In both cases, the maximum achievable  $f_{\text{O}_2}$ ,  $\sim \text{IW}-4.5$ , produces a maximum  $X_{\text{Fa}}$  before diffusion ceases that is a factor of  $>7$  less than would be required for UOC chondrule precursors, even for grains only  $0.1 \mu\text{m}$  in radius and nebular cooling times as high as  $10^6$  yr. The same dynamic models are also incapable of creating environments sufficiently oxidizing to produce olivine with  $X_{\text{Fa}} = 0.15$  during formation of chondrules by melting of FeO-poor precursors. If, instead, chondrule precursors were made of very FeO-rich, non-equilibrium condensates, reduction of chondrule melts by nebular gas



may have been arrested before the mean  $X_{\text{Fa}}$  of chondrule olivine could fall below 0.15 because chondrules were hot for such a short time. In contrast to the chondrules in unequilibrated ordinary chondrites, a nebular origin for the mineral assemblage of unequilibrated enstatite chondrites requires  $f_{\text{O}_2}$  significantly below that of a system of solar composition. In particular, after fractionation of specific amounts of predicted high-temperature condensates, equilibrium condensation in a system whose  $P^{\text{tot}} = 10^{-4}$  atm and whose initial composition is solar except for a C/O ratio of 0.83 yields an assemblage characterized by a very large enstatite/forsterite ratio, the presence of oldhamite and niningerite, metallic nickel-iron containing several wt% Si, and small amounts of pure silica and albitic plagioclase, very similar to the mineral assemblage of EH3 chondrites. Log  $f_{\text{O}_2}$  in this system varies from IW-8.9 at 1500 K to IW-13 at 900 K. The mechanisms proposed above for enriching nebular regions in oxygen relative to carbon produce other regions with complementary fractionations, but the latter are unsuitable sites for high-temperature condensation of EH3 chondrites because the very mechanism that separated oxygen from these sites left them vastly depleted in all condensable elements due to low-temperature condensation. It is seen that the mechanisms proposed to date for fractionation of C, O and H from one another are quantitatively insufficient to produce the magnitude of nebular  $f_{\text{O}_2}$  variations needed to account for primitive features of unequilibrated ordinary and enstatite chondrites. Perhaps it is time to consider the idea that the solar nebula inherited spatial heterogeneities in the relative proportions of these elements from its parent interstellar gas cloud, just as it did in the case of isotopic compositions.

#### ACKNOWLEDGMENTS

The experimental part of this paper is part of John Beckett's 1986 PhD thesis at the University of Chicago. The authors are grateful to A. Rubin for permission to use unpublished mineralogical data on EH3 chondrites, and to R. N. Clayton, J. N. Cuzzi, S. Desch, A. El Goresy, J. N. Grossman, I. Hutcheon, K. Keil, H. Palme, and Y. Lin for helpful discussions. The paper benefited from thorough reviews by H. C. Connolly, M. Petaev, and E. R. D. Scott. This research was supported by funds from the National Aeronautics and Space Administration through grants NNG05GG00G (to Lawrence Grossman) and NNG04GG14G (to Edward Stolper), and from the Carnegie Institution of Washington (to Fred Ciesla).

#### REFERENCES

- Alexander CMO, Hutchison R, Barber DJ (1989) Origin of chondrule rims and interchondrule matrices in unequilibrated ordinary chondrites. *Earth Planet Sci Lett* 95:187-207
- Allende Prieto C, Lambert DL, Asplund M (2001) The forbidden abundance of oxygen in the sun. *Astrophys J* 556:L63-L66
- Allende Prieto C, Lambert DL, Asplund M (2002) A reappraisal of the solar photospheric C/O ratio. *Astrophys J Lett* 573:L137-L140
- Anders E, Grevesse N (1989) Abundances of the elements: Meteoritic and solar. *Geochim Cosmochim Acta* 53:197-214
- Balbus SA, Hawley JF (1991) A powerful local shear instability in weakly magnetized disks. I - Linear analysis. II - Nonlinear evolution. *Astrophys J* 376:214-233
- Beckett JR, Live D, Tsay FD, Grossman L, Stolper E (1988)  $\text{Ti}^{3+}$  in meteoritic and synthetic hibonite. *Geochim Cosmochim Acta* 52:1479-1495
- Blum JD, Wasserburg GJ, Hutcheon ID, Beckett JR, Stolper EM (1989) Origin of opaque assemblages in C3V meteorites: Implications for nebular and planetary processes. *Geochim Cosmochim Acta* 53:543-556
- Boss AP (1998) Evolution of the solar nebula. IV. Giant gaseous protoplanet formation. *Astrophys J* 503:923-937
- Bottinga Y, Richet P (1978) Thermodynamics of liquid silicates, a preliminary report. *Earth Planet Sci Lett* 40:382-400
- Brearley AJ (1993) Matrix and fine-grained rims in the unequilibrated CO3 chondrite, ALHA77307: Origins and evidence for diverse, primitive nebular dust components. *Geochim Cosmochim Acta* 57:1521-1550

- Brearley AJ, Jones RH (1998) Chondritic meteorites. *Rev Mineral* 36:3-1--3-398
- Burns RG, Huggins FE (1973) Visible-region absorption spectra of a  $Ti^{3+}$  fassaite from the Allende meteorite: A discussion. *Am Mineral* 58:955-961
- Calvet N, Briceño C, Hernández J, Hoyer S, Hartmann L, Sicilia-Aguilar A, Megeath ST, D'Alessio P (2005) Disk evolution in the Orion OB1 association. *Astron J* 129:935-946
- Cassen P (2001) Nebular thermal evolution and the properties of primitive planetary materials. *Meteor Planet Sci* 36:671-700
- Charlu TV, Newton RC, Kleppa OJ (1981) Thermochemistry of synthetic  $CaAl_2SiO_7$  (gehlenite)- $Ca_2MgSi_2O_7$  (åkermanite) melilite. *Geochim Cosmochim Acta* 45:1609-1617
- Chase MW Jr (ed) (1998) NIST-JANAF Thermochemical Tables, fourth edition. *J Phys Chem Ref Data*, Monograph No. 9
- Chizmadia LJ, Rubin AE, Wasson JT (2002) Mineralogy and petrology of amoeboid olivine inclusions in CO3 chondrites: Relationship to parent-body aqueous alteration. *Meteor Planet Sci* 37:1781-1796
- Ciesla FJ, Cuzzi JN (2006) The evolution of the water distribution in a viscous protoplanetary disk. *Icarus* 181:178-204
- Clayton RN (2005) Disequilibrium oxygen chemistry in the solar nebula. *Lunar Planet Sci XXXVI*:1711
- Connolly HC Jr, Hewins RH, Ash RD, Zanda B, Lofgren GE, Bourot-Denise M (1994) Carbon and the formation of reduced chondrules. *Nature* 371:136-139
- Cuzzi JN, Alexander CMO'D (2006) Chondrule formation in particle-rich nebular regions at least hundreds of kilometres across. *Nature* 441:483-485
- Cuzzi JN, Zahnle KJ (2004) Material enhancement in proto protoplanetary nebulae by particle drift through evaporation fronts. *Astrophys J* 614:490-496
- Davis AM, Hashimoto A, Clayton RN, Mayeda TK (1990) Isotope mass fractionation during evaporation of  $Mg_2SiO_4$ . *Nature* 347:655-658
- Davis AM, Tanaka T, Grossman L, Lee T, Wasserburg GJ (1982) Chemical composition of HAL, an isotopically-unusual Allende inclusion. *Geochim Cosmochim Acta* 46:1627-1651
- Dowty E, Clark JR (1973) Crystal structure refinement and optical properties of a  $Ti^{3+}$  fassaite from the Allende meteorite. *Am Mineral* 58:230-242
- Dubrulle B, Marie L, Normand C, Richard D, Hersant F, Zahn J-P (2005) An hydrodynamic shear instability in stratified disks. *Astron Astrophys* 429:1-13
- Dubrulle B, Morfill GE, Sterzik M (1995) The dust sub-disk in the protoplanetary nebula. *Icarus* 114:237-246
- Ebel DS, Alexander CMO'D (2005) Condensation from cluster-IDP enriched vapor inside the snow line: Implications for Mercury, asteroids, and enstatite chondrites. *Lunar Planet Sci XXXVI*:1797
- Ebel DS, Grossman L (2000) Condensation in dust-enriched systems. *Geochim Cosmochim Acta* 64:339-366
- Ebel DS, Grossman L (2001) Condensation from supernova gas made of free atoms. *Geochim Cosmochim Acta* 65:469-477
- El Goresy A, Nagel K, Ramdohr P (1978) Fremdlinge and their noble relatives. In: *Proc 9th Lunar Planet Sci Conf*. Pergamon, New York, p 1279-1303
- Fedkin AV, Grossman L (2006) The fayalite content of chondritic olivine: Obstacle to understanding the condensation of rocky material. In: *Meteorites and the Early Solar System II*. Lauretta DS, McSween HY Jr (eds) University of Arizona Press, Tucson, p 279-294
- Fedkin AV, Grossman L, Ghiorso MS (2006) Model evaporation of chondrule precursors in nebular shocks. *Lunar Planet Sci XXXVII*:2249
- Fegley B Jr, Palme H (1985) Evidence for oxidizing conditions in the solar nebula from Mo and W depletions in refractory inclusions in carbonaceous chondrites. *Earth Planet Sci Lett* 72:311-326
- Gammie CF (2001) Nonlinear outcome of gravitational instability in cooling, gaseous disks. *Astrophys J* 553:174-183
- Gasparik T, Lindsley DH (1980) Phase equilibria at high pressures of pyroxenes containing monovalent and trivalent ions. *Rev Mineral* 7:309-339
- Goldreich P, Lynden-Bell D (1965) II. Spiral arms as sheared gravitational instabilities. *Monthly Notices R Ast Soc* 130:125-158
- Grossman JN, Brearley AJ (2005) The onset of metamorphism in ordinary and carbonaceous chondrites. *Meteoritics Planet Sci* 40:87-122
- Grossman L, Ebel DS, Simon SB, Davis AM, Richter FM, Parsad NM (2000) Major element chemical and isotopic compositions of refractory inclusions in C3 chondrites: The separate roles of condensation and evaporation. *Geochim Cosmochim Acta* 64:2879-2894
- Grossman L, Ganapathy R, Davis AM (1977) Trace elements in the Allende meteorite-III. Coarse-grained inclusions revisited. *Geochim Cosmochim Acta* 41:1647-1664
- Grossman L, Olsen E, Lattimer JM (1979) Silicon in carbonaceous chondrite metal: Relic of high-temperature condensation. *Science* 206:449-451
- Grossman L, Steele IM (1976) Amoeboid olivine aggregates in the Allende meteorite. *Geochim Cosmochim Acta* 40:149-155

- Helffrich G, Wood B (1989) Subregular model for multicomponent solutions. *Am Mineral* 74:1016-1022
- Holzheid A, O'Neill HStC (1995) The Cr-Cr<sub>2</sub>O<sub>3</sub> oxygen buffer and the free energy of formation of Cr<sub>2</sub>O<sub>3</sub> from high-temperature electrochemical measurements. *Geochim Cosmochim Acta* 59:475-479
- Huss GR, Keil K, Taylor GJ (1981) The matrices of unequilibrated ordinary chondrites: implications for the origin and history of chondrites. *Geochim Cosmochim Acta* 45:33-51
- Hutson M, Ruzicka A (2000) A multi-step model for the origin of E3 (enstatite) chondrites. *Meteor Planet Sci* 35:601-608
- Ihinger PD, Stolper E (1986) The color of meteoritic hibonite: an indicator of oxygen fugacity. *Earth Planet Sci Lett* 78:67-79
- Johnson MC (1986) The solar nebula redox state as recorded by the most reduced chondrules of five primitive chondrites. *Geochim Cosmochim Acta* 50:1497-1502
- Jones RH (1990) Petrology and mineralogy of Type II, FeO-rich chondrules in Semarkona (LL3.0): Origin by closed-system fractional crystallization, with evidence for supercooling. *Geochim Cosmochim Acta* 54:1785-1802
- Jones RH, Danielson LR (1997) A chondrule origin for dusty relict olivine in unequilibrated chondrites. *Meteor Planet Sci* 32:753-760
- Krot AN, Fagan TJ, Keil K, McKeegan KD, Sahijpal S, Hutcheon ID, Petaev MI, Yurimoto H (2004a) Ca, Al-rich inclusions, amoeboid olivine aggregates, and Al-rich chondrules from the unique carbonaceous chondrite Acfer 094: I. Mineralogy and petrology. *Geochim Cosmochim Acta* 68:2167-2184
- Krot AN, Fegley B Jr, Lodders K, Palme H. (2000) Meteoritical and astrophysical constraints on the oxidation state of the solar nebula. In: Protostars and Planets IV. Mannings V, Boss A, Russell SS (eds) University of Arizona Press, Tucson, p 1019-1054
- Krot AN, Petaev MI, Russell SS, Itoh S, Fagan TJ, Yurimoto H, Chizmadia L, Weisberg MK, Komatsu M, Ulyanov AA, Keil K (2004b) Amoeboid olivine aggregates and related objects in carbonaceous chondrites: records of nebular and asteroid processes. *Chemie der Erde* 64:185-239
- Larimer JW (1975) The effect of C/O ratio on the condensation of planetary material. *Geochim Cosmochim Acta* 39:389-392
- Larimer JW, Anders E (1970) Chemical fractionations in meteorites-III. Major element fractionations in chondrites. *Geochim Cosmochim Acta* 34:367-387
- Larimer JW, Bartholomay M (1979) The role of carbon and oxygen in cosmic gases: some applications to the chemistry and mineralogy of enstatite chondrites. *Geochim Cosmochim Acta* 43:1455-1466
- Lauretta DS, Buseck PR, Zega TJ (2001) Opaque minerals in the matrix of the Bishunpur (LL3.1) chondrite: Constraints on the chondrule formation environment. *Geochim Cosmochim Acta* 65:1337-1353
- Leroux H, Libourel G, Lemelle L, Guyot F (2003) Experimental study and TEM characterization of dusty olivines in chondrites: Evidence for formation by in situ reduction. *Meteor Planet Sci* 38:81-94
- Lin DNC, Papaloizou J (1980) On the structure and evolution of the primordial solar nebula. *Mon Not R Ast Soc* 191:37-48
- Lusby D, Scott ERD, Keil K (1987) Ubiquitous high-FeO silicates in enstatite chondrites. *Proc 17th Lunar Planet Sci Conf, Part 2, J Geophys Res* 92:E679-E695
- Lyons JR (2006) Photooxidation in the inner solar nebula. *Lunar Planet Sci XXXVII*:2374
- MacPherson GJ, Bar-Matthews M, Tanaka T, Olsen E, Grossman L (1983) Refractory inclusions in the Murchison meteorite. *Geochim Cosmochim Acta* 47:823-839
- MacPherson GJ, Grossman L, Allen JM, Beckett JR (1981) Origin of rims on coarse-grained inclusions in the Allende meteorite. *Proc Lunar Planet Sci Conf, 12B*. Pergamon, New York, p 1079-1091
- MacPherson GJ, Grossman L, Hashimoto A, Bar-Matthews M, Tanaka T (1984a) Petrographic studies of refractory inclusions from the Murchison meteorite. *Proc 15th Lunar Planet Sci Conf, Part 1, J Geophys Res* 89 Supp:C299-C312
- MacPherson GJ, Krot AN (2002) Distribution of Ca-Fe-silicates in CV3 chondrites: Possible controls by parent-body compaction. *Meteor Planet Sci* 37 Supp:A91
- MacPherson GJ, Paque JM, Stolper E, Grossman L (1984b) The origin and significance of reverse zoning in melilite from Allende Type B inclusions. *J Geol* 92:289-305
- McCoy TJ, Scott ERD, Jones RH, Keil K, Taylor GJ (1991) Composition of chondrule silicates in LL3-5 chondrites and implications for their nebular history and parent body metamorphism. *Geochim Cosmochim Acta* 55:601-619
- Myers J, Eugster HP (1983) The system Fe-Si-O: Oxygen buffer calibrations to 1,500 K. *Contrib Mineral Petrol* 82:75-90
- Nagahara H (1981) Evidence for secondary origin of chondrules. *Nature* 292:135-136
- Nehru CE, Prinz M, Weisberg MK, Delaney JS (1984) Parsa: an unequilibrated enstatite chondrite (UEC) with an aubrite-like impact melt clast. *Lunar Planet Sci XV*:597-598
- Palme H, Fegley B Jr (1990) High-temperature condensation of iron-rich olivine in the solar nebula. *Earth Planet Sci Lett* 101:180-195

- Palme H, Hutcheon ID, Spettel B (1994) Composition and origin of refractory-metal-rich assemblages in a Ca, Al-rich Allende inclusion. *Geochim Cosmochim Acta* 58:495-513
- Perry RH, Chilton CH (1973) *Chemical Engineers Handbook*, fifth edition. McGraw-Hill, New York
- Petaev MI (2006) Modeling major and trace element chemistry of zoned metal grains from the CH and CB chondrites. *Lunar Planet Sci XXXVII*:1681
- Petaev MI, Wood JA (1998) The condensation with partial isolation (CWPI) model of condensation in the solar nebula. *Meteoritics Planet Sci* 33:1123-1137
- Petaev MI, Wood JA, Meibom A, Krot AN, Keil K (2003) The ZONMET thermodynamic and kinetic model of metal condensation. *Geochim Cosmochim Acta* 67:1737-1751
- Prinn RG, Fegley B Jr. (1989) Solar nebula chemistry: Origin of planetary, satellite, and cometary volatiles. In: *Origin and Evolution of Planetary and Satellite Atmospheres*. Atreya SK, Pollack JB, Matthews MS (eds) University Arizona Press, Tucson, p 78-136
- Rambaldi ER (1981) Relict grains in chondrules. *Nature* 293:558-561
- Reed SJB, Ware NG (1973) Quantitative electron microprobe analysis using a lithium drifted silicon detector. *X-Ray Spectrom* 2:69-74
- Rietmeijer FJM (1998) Interplanetary dust particles. *Rev Mineral* 36:2-1—2-95
- Ruzicka A (1997) Mineral layers around coarse-grained, Ca-Al-rich inclusions in CV3 carbonaceous chondrites: Formation by high-temperature metasomatism. *J Geophys Res* 102:13387-13402
- Sakao H, Elliott JF (1975) Thermodynamics of dilute bcc Fe-Si alloys. *Metall Trans* 6A:1849-1851
- Scott ERD, Taylor GJ (1983) Chondrules and other components in C, O, and E chondrites: Similarities in their properties and origins. *Proc 14th Lunar Planet Sci Conf, Part 1, J Geophys Res* 88 Supp:B275-B286
- Shu FH, Shang H, Gounelle M, Glassgold AE, Lee T (2001) The origin of chondrules and refractory inclusions in chondritic meteorites. *Astrophys J* 548:1029-1050
- Simon JJ, Young ED, Russell SS, Tonui EK, Dyl KA, Manning CE (2005) A short timescale for changing oxygen fugacity in the solar nebula revealed by high-resolution 26Al-26Mg dating of CAI rims. *Earth Planet Sci Lett* 238:272-283
- Simon SB, Davis AM, Grossman L (1999) Origin of compact type A refractory inclusions from CV3 carbonaceous chondrites. *Geochim Cosmochim Acta* 63:1233-1248
- Simon SB, Grossman L (2004) A preferred method for the determination of bulk compositions of coarse-grained refractory inclusions and some implications of the results. *Geochim Cosmochim Acta* 68:4237-4248
- Simon SB, Grossman L (2006) A comparative study of melilite and fassaite in Types B1 and B2 refractory inclusions. *Geochim Cosmochim Acta* 70:780-798
- Simon SB, Grossman L, Davis AM (1991) Fassaite composition trends during crystallization of Allende Type B refractory inclusion melts. *Geochim Cosmochim Acta* 55:2635-2655
- Simon SB, Sutton SR, Grossman L (2005) Valence of Ti and V in fassaite: A recorder of oxygen fugacity during crystallization of coarse-grained refractory inclusions. *Workshop on Oxygen in the Earliest Solar System, LPI Contrib* 1278:35
- Simon SB, Sutton SR, Grossman L (2007) Valence of titanium and vanadium in pyroxene in refractory inclusion interiors and rims. *Geochim Cosmochim Acta* 71:3098-3118
- Stolper E (1982) Crystallization sequences of Ca-Al-rich inclusions from Allende: An experimental study. *Geochim Cosmochim Acta* 46:2159-2180
- Stolper E, Paque JM (1986) Crystallization sequences of Ca-Al-rich inclusions from Allende: The effects of cooling rate and maximum temperature. *Geochim Cosmochim Acta* 50:1785-1806
- Sutton SR, Karner J, Papike J, Delaney JS, Shearer C, Newville M, Eng P, Rivers M, Dyar MD (2005) Vanadium K edge XANES of synthetic and natural basaltic glasses and application to microscale oxygen barometry. *Geochim Cosmochim Acta* 69:2333-2348
- Vogel IA, Palme H (2004) Activity coefficients of silicon in iron-nickel alloys: Experimental determination and relevance for planetary differentiation. *Lunar Planet Sci XXXV*:1592
- Wang J, Davis AM, Clayton RN, Mayeda TK, Hashimoto A (2001) Chemical and isotopic fractionation during the evaporation of the FeO-MgO-SiO<sub>2</sub>-CaO-Al<sub>2</sub>O<sub>3</sub>-TiO<sub>2</sub> rare earth element melt system. *Geochim Cosmochim Acta* 65:479-494
- Wark DA, Boynton WV (2001) The formation of rims on calcium-aluminum-rich inclusions: Step I-Flash heating. *Meteoritics Planet Sci* 36:1135-1166
- Wark DA, Lovering JF (1977) Marker events in the early evolution of the solar system: Evidence from rims on Ca-Al-rich inclusions in carbonaceous chondrites. *Proc Lunar Sci Conf 8th*, Pergamon, New York, p 95-112
- Wasson JT (1985) *Meteorites: Their Record of Early Solar-System History*. WH Freeman and Co., New York
- Weisberg MK, Prinz M, Fogel RA (1994) The evolution of enstatite and chondrules in unequilibrated enstatite chondrites: Evidence from iron-rich pyroxene. *Meteoritics* 29:362-373
- Williams RJ, Mullins O (1976) A system using solid ceramic oxygen electrolyte cells to measure oxygen fugacities in gas-mixing systems. *NASA Tech. Mem.* X-58167

- Wood JA (1967) Olivine and pyroxene compositions in type II carbonaceous chondrites. *Geochim Cosmochim Acta* 31:2095-2108
- Wood JA (2004) Formation of chondritic refractory inclusions: the astrophysical setting. *Geochim Cosmochim Acta* 68:4007-4021
- Yoneda S, Grossman L (1995) Condensation of CaO-MgO-Al<sub>2</sub>O<sub>3</sub>-SiO<sub>2</sub> liquids from cosmic gases. *Geochim Cosmochim Acta* 59:3413-3444
- Zanda B, Bourot-Denise M, Perron C, Hewins RH (1994) Origin and metamorphic redistribution of silicon, chromium, and phosphorus in the metal of chondrites. *Science* 265:1846-1849